Archive of Applied Mechanics (2026) 96:86
https://doi.org/10.1007/s00419-026-03071-y

ORIGINAL

Fatih Uzun · Alexander M. Korsunsky

A closed-form eigenstrain framework for classical springback in inelastically bent beams

Received: 18 September 2025 / Revised: 10 February 2026 / Accepted: 20 March 2026

Abstract Springback of prismatic beams following inelastic bending is a classical problem in engineering plasticity, with benchmark closed-form solutions available for canonical cross sections under elastic–perfectly plastic assumptions. Here, the same bending–unloading problem is reformulated systematically within the eigenstrain framework by treating the plastic strain accumulated during loading as a retained inelastic strain source after unloading. This recasts the post-unloading configuration as a residual stress problem driven by retained inelastic strains, yielding a unified analytical route to residual curvature, residual elastic strain, and self-equilibrated residual stress distributions. Closed-form expressions are derived for rectangular, circular, and I-shaped sections and implemented in MATLAB to compare moment–curvature response, springback magnitude, and residual-field characteristics across geometries. The closed-form results are verified against an independent classical beam-plasticity benchmark based on piecewise elastic–perfectly plastic stress blocks integrated over the section and elastic unloading via sectional stiffness, showing excellent agreement in both the elastic and post-yield regimes. The formulation embeds classical springback results within an eigenstrain-based residual-stress viewpoint and provides a transparent analytical baseline for geometry comparisons and future extensions through more general eigenstrain inputs.

Keywords Closed-form solution · Eigenstrain theory · Springback · Beam bending · Residual stress · Moment–curvature relationship

1 Introduction

Residual stresses are the internal stresses locked into a material after its fabrication, existing in the absence of any external load [1, 2]. They arise from nonuniform inelastic deformation and/or thermal gradients introduced during processes such as forming [3–5], welding [6–12], machining [13, 14], or heat-treatment [15–18]. In general, tensile residual stresses can be detrimental by promoting crack initiation and reducing fatigue life [19–22], whereas compressive residual stresses are often beneficial by inhibiting crack growth and improving fatigue resistance [23–26]. Residual stresses can also affect dimensional stability [27–30], corrosion resistance [31–34], distortion [35–38], crack delamination [39, 40], and other performance aspects [41–44]. They are self-balanced (self-equilibrating) within the body [8, 45], so that tensile regions are compensated by compression elsewhere [46]. Residual stresses are commonly classified by scale into Type I (macro-scale), Type II (inter-granular), and Type III (intragranular) components [47–50]. In addition, their sign (tensile vs. compressive) is critical because it strongly influences fatigue and fracture behaviour.

F. Uzun (✉)
Department of Engineering Science, University of Oxford, Oxford, UK
e-mail: fatihuzun@me.com; fatih.uzun@eng.ox.ac.uk

A. M. Korsunsky
Trinity College, Oxford, UK

Published online: 10 April 2026

Analytical modelling remains a cornerstone of engineering mechanics because it provides tractable, closed-form insight into problems ranging from beam bending [51] and torsion [52, 53] to thermal expansion [54–56] and stress concentrations [57–60]. Classical formulations such as Euler–Bernoulli and Timoshenko beam theories are still widely used to predict load–deflection and stress–strain responses under elastic or piecewise linear elastic–plastic assumptions [61], and they continue to underpin applications in civil structures [62, 63], aerospace components [64], layered composites [65, 66], and coatings [67]. Beyond direct structural response, analytical approaches are also valuable for interpreting and bounding residual stress fields [68] and their mechanical consequences [69, 70], and for describing unloading and recovery effects in inelastic deformation problems [71], including strain recovery phenomena such as springback [72].

Eigenstrain theory [73], first introduced by Mura [74], provides a rigorous framework for representing residual stress as the elastic response to incompatible inelastic strains (eigenstrains) that are locked in after processing. In the forward setting, prescribed eigenstrain distributions can be used to predict residual stress fields produced by a wide range of inelastic mechanisms [75–80]. In the inverse setting, eigenstrain offers an efficient basis for reconstructing residual stress from partial measurements by identifying the underlying eigenstrain field [81–87]. This combination, physically transparent internal sources together with a compact mathematical representation, has made eigenstrain approaches attractive for residual-stress analysis across diverse applications.

The problem of springback in beams subjected to inelastic bending has a long history in engineering plasticity, with early and continuing treatments of elastic–plastic bending and unloading [88, 89]. Under simplifying material assumptions, closed-form solutions describing moment–curvature response and post-unloading curvature have been developed and consolidated in classical works [90, 91]. For common cross sections, such as rectangular beams, circular rods, and I-sections, explicit expressions for springback curvature and related quantities are available [92, 93], and they remain standard references in engineering plasticity [92].

Despite the maturity of the classical literature, springback is typically presented as a plastic-bending/unloading calculation rather than as an eigenstrain-driven residual-field problem [94–96]. Meanwhile, eigenstrain methods are widely used for residual-stress modelling and reconstruction, and bending is often discussed as a convenient setting for illustrating eigenstrain concepts [97, 98]. However, the specific springback problem is not treated in a systematic, beam-theory, closed-form manner within a unified eigenstrain formulation. This leaves a gap between classical springback solutions for canonical sections and eigenstrain-based residual-stress mechanics where the link is conceptually natural, unloading is elastic with internal inelastic sources, but it is not usually made explicit as a consistent analytical workflow that yields residual curvature, residual elastic strain, and residual stress in one framework.

Building on the classical springback literature, this study formulates beam springback within an explicit, systematic eigenstrain workflow that is readily reusable. The eigenstrain viewpoint separates the generation of inelastic strain during loading from the elastic residual problem after unloading. Once the retained inelastic strain field is known whether from a closed-form plasticity model, a finite-element simulation [99], or inverse identification from measurements [100, 101], the unloading stage is treated not as a separate recovery calculation, but as a direct consequence of the retained field. This unifies the determination of residual curvature and stress into a single consistency check. In doing so, plastic strain generated during loading is treated as an eigenstrain field that persists upon unloading, so the post-unloading configuration is obtained from elastic equilibrium and compatibility with internal sources.

The specific contributions of this paper are fourfold. A compact beam-level eigenstrain workflow for springback is presented with explicit compatibility and equilibrium statements. Closed-form expressions are derived for residual curvature, residual elastic strain, and residual stress for three canonical cross sections, that are rectangular, circular, and I-shaped, under elastic–perfectly plastic response. A geometry-consistent comparison is provided of plastic penetration, elastic recovery, and residual-field magnitudes under identical assumptions. The closed-form eigenstrain results are verified against an independent classical elastoplastic benchmark, together with a yield-strain parametric sensitivity study.

The remainder of the paper proceeds as follows. Section 2 formulates inelastic bending and springback within the eigenstrain framework by identifying the loading-stage plastic strain as a retained eigenstrain field and posing the unloaded configuration as an elastic equilibrium problem with internal strain sources, yielding closed-form expressions for the moment–curvature response and for residual curvature, strain relaxation, and residual stress for rectangular, circular, and I-shaped cross sections under elastic–perfectly plastic response. Section 3 implements these expressions to compare geometry effects on plastic penetration, elastic recovery, and residual-field characteristics under consistent assumptions. Section 4 verifies the closed-form eigenstrain results against an independent classical benchmark based on standard piecewise stress distributions and elastic

unloading via sectional stiffness, and presents a yield-strain parametric sensitivity study. Section 5 summarizes the main findings, key limitations of the present assumptions, and avenues for extension through more general eigenstrain inputs.

2 Eigenstrain formulation for inelastic bending and springback

This section formulates inelastic bending and springback within the eigenstrain framework, specializing the general results to rectangular, circular, and I-shaped cross sections. By identifying the plastic strain generated during loading as a locked-in eigenstrain field, the derivation yields closed-form expressions for the resulting residual curvature, residual elastic strain, and self-equilibrated stress distributions. In eigenstrain theory, an eigenstrain is any permanent inelastic strain that is not itself stress-producing, but which generates residual elastic strains and stresses through compatibility and equilibrium constraints. In the present bending problem, the eigenstrain is taken to be the plastic strain distribution accumulated during loading. This viewpoint does not replace classical elastoplastic bending; rather, it recasts springback as residual-stress mechanics. Once the eigenstrain is prescribed, the post-unloading state is obtained from elastic relations plus the requirement that internal forces and moments satisfy equilibrium in the absence of external loading. This is particularly convenient for prismatic beams, where geometry allows analytical integration and direct comparison across different cross sections.

In the present paper, the material response during loading is taken as isotropic linear elasticity with elastic–perfectly plastic yielding. This choice is made deliberately to keep the subsequent eigenstrain-driven unloading stage fully analytical and to isolate the central conceptual point. Once the inelastic strain field is fixed, springback and residual stresses follow from elastic compatibility and equilibrium with internal strain sources. In this setting, the eigenstrain framework does not compete with classical incremental plasticity; rather, it provides a clear residual-stress interpretation of the unloading problem while retaining the well-known closed-form benchmark character of beam solutions.

It is important to note that strain hardening primarily affects the shape of the accumulated inelastic strain distribution through the section during loading. In an eigenstrain formulation, this influence enters through the prescribed eigenstrain field. If hardening leads to a nonlinear or non-piecewise-linear eigenstrain distribution, the same unloading relations remain valid, but the resulting sectional integrals may no longer admit compact closed-form expressions. Therefore, hardening is not excluded by the framework; rather, it shifts the problem from closed-form evaluation to numerical quadrature, or symbolic evaluation where possible, once the eigenstrain field is specified.

Accordingly, the present work focuses on the elastic–perfectly plastic case as a canonical baseline that permits closed-form expressions for residual curvature, residual elastic strain, and residual stress across common section geometries. More general constitutive behaviour, including hardening, anisotropy, and rate dependence, can be incorporated at the level of the eigenstrain input, either from an incremental constitutive model, from numerical simulation, or from inverse identification, while the unloading stage remains an elastic eigenstrain problem governed by the same equilibrium constraints.

2.1 Governing assumptions, compatibility, and equilibrium

The analysis assumes prismatic beams in small-strain kinematics under pure bending in the sense of Euler–Bernoulli theory that state plane cross sections remain plane and perpendicular to the neutral axis, and shear deformation is neglected. The material is modelled as isotropic linear elasticity combined with elastic–perfectly plastic response during loading. Symmetry about the neutral axis is used for the presented cross sections so that the neutral axis remains at the geometric mid-plane, unless stated otherwise, and the plastic zones develop symmetrically about the line parallel to z-axis where y is 0.

Compatibility in Euler–Bernoulli bending implies a linear total axial strain field through the thickness, $\varepsilon^T(y) \propto y$. In the eigenstrain setting, the total strain is decomposed into elastic strain and an inelastic (eigenstrain) part. The eigenstrain field is allowed to be piecewise, elastic core plus plastified zones, but the total strain remains linear along the beam height, y, so the residual elastic strain that produces residual stress is whatever is required to reconcile the linear total strain with the prescribed eigenstrain distribution.

Equilibrium is enforced through the standard sectional resultants. During loading, the stress distribution over the cross section must generate an internal bending moment that balances the applied moment. During

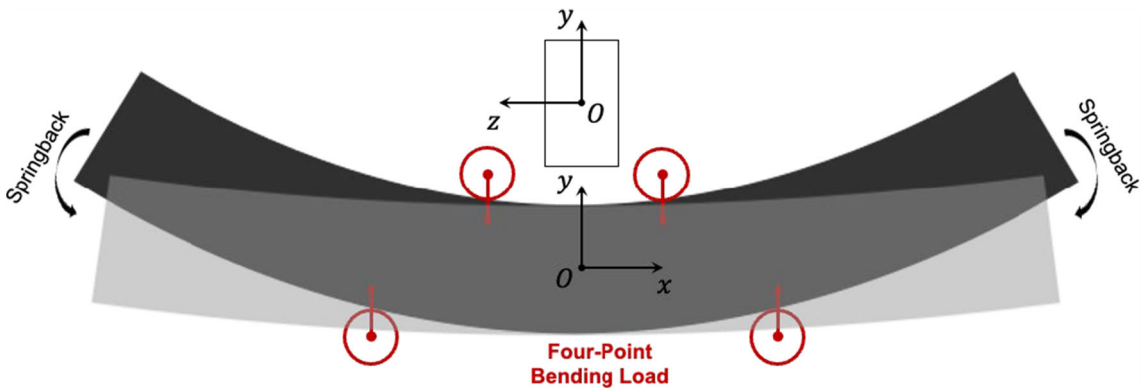

Fig. 1 Schematic of a beam subjected to bending and subsequent unloading. Plastic strains accumulate near the outer regions during loading and upon unloading, elastic recovery produces springback while the locked-in plastic strain field leaves a permanent curvature and a self-equilibrated residual stress state

unloading (springback), the applied moment is removed; therefore, the residual stress field must be self-equilibrated so that it produces no net bending moment. For the symmetric sections considered here under pure bending, the axial force resultant also vanishes by symmetry. For asymmetric sections, enforcing zero axial force provides an additional condition that is required to determine the neutral axis position and the residual curvature in a consistent manner.

In the general three-dimensional eigenstrain theory, a prescribed eigenstrain field is in general incompatible with a globally continuous displacement field and may be represented through incompatibility measures, via an incompatibility tensor, and/or stress-function approaches. In the present study, the treatment is intentionally specialized to the one-dimensional Euler–Bernoulli beam setting, where the relevant compatibility requirement is the linear through-thickness total strain and the residual elastic field is determined by enforcing sectional equilibrium, zero net moment after unloading, and zero net axial force where applicable. Thus, the beam formulation used here may be viewed as the reduced, sectional form of the general eigenstrain concept, expressed directly in terms of compatibility of the beam kinematics and equilibrium of resultants.

The bending problem is formulated by decomposing the total strain into elastic and inelastic (eigenstrain) components, as illustrated in Fig. 1. During the loading phase, total axial strain varies linearly through the thickness, generating piecewise plastic strains in the outer regions where the yield limit is exceeded. Upon unloading, these plastic strains are retained as a permanent eigenstrain field. The beam relaxes elastically to a new equilibrium curvature, visualized in the schematic as the transition from the loaded shape to the springback shape, governed by the internal balance of residual stresses.

The total axial strain, $\varepsilon^T(y)$, distribution in a beam subjected to pure bending is given by Eq. 1, where the strain at any vertical position, y, within the cross section is assumed to vary linearly. Here, κ denotes the curvature during loading, such that the total strain varies proportionally with the distance from the neutral axis. This expression reflects the classical assumption of plane sections remaining plane and perpendicular to the neutral axis, a fundamental principle of Euler–Bernoulli beam theory. The total strain is decomposed into elastic $\varepsilon^e(y)$ and $\varepsilon^p(y)$ plastic components, thereby providing a foundation for analysing both the recoverable and irreversible parts of the deformation during inelastic bending.

$$\varepsilon^T(y) = \varepsilon^e(y) + \varepsilon^p(y) = \kappa y \tag{1}$$

The elastic strain component, which governs stress generation through Hooke's law, is obtained by subtracting the plastic strain from the total strain, as expressed in Eq. 2 in terms of the residual curvature, κ_r. Accordingly, in regions where plasticity develops, the elastic strain and the stress is reduced. This formulation is central to identifying the stress distribution during the loading phase and directly influences the resulting internal bending moment.

$$\varepsilon^e(y) = \kappa y - \varepsilon^p(y) \tag{2}$$

The distribution of plastic strain across the beam height, regarding the elastic-core height, h_e, is defined in piecewise form in Eq. 3, distinguishing between the elastic core and plastified outer zones. Within the central region $|y| < h_e$, the material remains elastic, while in the outer regions $|y| \geq h_e$, plastic strain accumulates

linearly. This representation ensures continuity and symmetry about the neutral axis and is consistent with an elastic-perfectly plastic material model under bending.

$$\varepsilon^p(y) = \begin{cases} \kappa(y + h_e), & y \le -h_e \\ 0, & -h_e < y < h_e \\ \kappa(y - h_e), & y \ge h_e \end{cases} \tag{3}$$

The curvature, κ, at the onset of yielding is related to the material's yield strain, ε_y, and the elastic-core height, h_e, via Eq. 4. This relationship provides a direct geometric-material link, establishing how increased curvature reduces the size of the elastic region as yielding progresses. This expression is particularly important for tracking the plastic front and quantifying the evolution of plasticity with increasing applied moment.

$$\kappa = \frac{\varepsilon_y}{h_e} \tag{4}$$

To model unloading within eigenstrain theory, the eigenstrain, $\varepsilon^*(y)$, is introduced as a stress-free inelastic strain field that remains in the material after removal of external loads. Eigenstrain does not generate stress by itself; instead, residual stresses arise from the elastic strain required to accommodate a prescribed eigenstrain distribution while satisfying equilibrium and compatibility. Under the present elastic–perfectly plastic bending model, the retained inelastic strain is the plastic strain accumulated during loading. Accordingly, the eigenstrain in the unloaded configuration is identified with the plastic strain distribution, $\varepsilon^p(y)$, obtained from the loading solution given in Eq. 3.

$$\varepsilon^*(y) = \varepsilon^p(y) \tag{5}$$

Although eigenstrain is stress-free by definition, it is generally not compatible with the kinematics of the unloaded beam. After unloading, the beam must satisfy Euler–Bernoulli kinematics, so the total axial strain varies smoothly and linearly through the thickness. In contrast, the retained inelastic strain left by plastic bending is typically nonuniform and can change form across elastic and plastified regions. This mismatch cannot be accommodated by a single compatible displacement field, so an additional elastic strain must develop to enforce compatibility and equilibrium, which in turn produces a self-equilibrated residual stress field.

Following unloading, the total strain distribution is again assumed to be linear and is described by Eq. 6, where κ_r denotes the residual curvature. This total strain is the sum of the residual elastic strain, $\varepsilon^r(y)$, and the eigenstrain, $\varepsilon^*(y)$. With eigenstrain prescribed by Eq. 5, the unloaded state is solved as an elastic equilibrium/compatibility problem with internal strain sources. This formulation captures the final strain state of the beam and is key to characterizing the springback response resulting from elastic recovery.

$$\varepsilon^T(y) = \varepsilon^r(y) + \varepsilon^*(y) = \kappa_r y \tag{6}$$

The residual elastic strain, $\varepsilon^r(y)$, that gives rise to self-equilibrated residual stresses in the unloaded beam is isolated in Eq. 7. This expression quantifies how the beam internally accommodates the eigenstrain distribution after removal of external loads, and is essential for computing the internal moment and stress profiles in the unloaded configuration.

$$\varepsilon^r(y) = \kappa_r y - \varepsilon^*(y) \tag{7}$$

To quantify the extent of elastic strain released, $\delta\varepsilon(y)$, during unloading, the strain relaxation is defined in Eq. 8 as the difference between the elastic strain, $\varepsilon^e(y)$, during loading and the residual elastic strain, $\varepsilon^r(y)$, after unloading. This measure characterizes the transition between the loaded and unloaded states and provides insight into the redistribution of internal stresses due to elastic recovery.

$$\delta\varepsilon(y) = \varepsilon^e(y) - \varepsilon^r(y) \tag{8}$$

By substituting the definitions of $\varepsilon^e(y)$ and $\varepsilon^r(y)$, and noting the identity given in Eq. 5, the strain relaxation simplifies to Eq. 9. This result confirms that the difference in curvature before and after unloading governs the elastic recovery profile, and that the strain relaxation maintains a linear variation through the beam height. This equation sets the stage for deriving expressions for springback and residual moment in later sections.

$$\delta\varepsilon(y) = (\kappa - \kappa_r)y \tag{9}$$

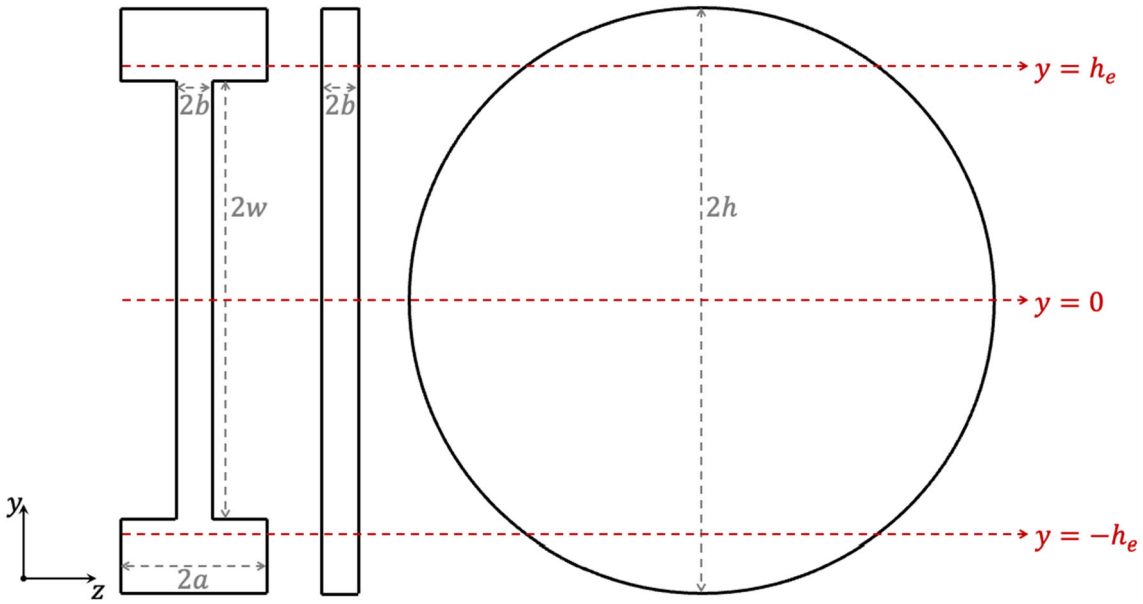

Fig. 2 Rectangular, circular, and I-shaped cross sections with the geometric parameters used in the closed-form eigenstrain-based bending and springback expressions

Equation 9 shows that the strain relaxation is linear through the thickness and depends only on the curvature recovery. This is useful because, once the residual curvature is determined for a given cross section, the released elastic strain and the residual stress distribution follow directly without additional incremental modelling and the geometry enters only through the sectional integrals used to enforce the unloaded equilibrium condition.

The relations above provide a general eigenstrain-based backbone for inelastic bending and springback that are a piecewise eigenstrain field is prescribed from the loading stage, the unloaded state is expressed as a linear total strain combined with the retained eigenstrain, and the residual curvature is determined from moment equilibrium in the unloaded configuration. The following subsections apply this strategy to rectangular, circular, and I-shaped cross sections illustrated in Fig. 2. In each case, the elastoplastic state is parameterized by the elastic-core height and the resulting expressions connect curvature, yield strain, and geometry to the moment–curvature response, springback, and residual elastic strain distributions.

2.2 Rectangular beam

Rectangular beams provide the simplest setting for illustrating the eigenstrain interpretation of springback, because the cross-sectional partitions cleanly into an elastic core and two symmetric plastified layers. The closed-form solution clarifies how the penetration of the plastic front governs both the nonlinear moment–curvature response during loading and the residual curvature after unloading. Moment expressions are derived by integrating the stress resultants over the elastic and plastified regions, and then obtains springback by enforcing zero net internal moment in the unloaded configuration.

Equation 10 represents the general expression for the internal bending moment, M, in a rectangular beam cross section subjected to inelastic deformation, formulated within the eigenstrain framework. The moment is calculated by integrating the product of stress and moment arm across the entire cross-sectional area. Since the stress is described by Hooke's law, and the moment arm, y, the integrand becomes $E\left(\varepsilon^T - \varepsilon^*\right)y$ where E is the elastic modulus. The cross section is partitioned into three regions that are the upper plastic zone, the central elastic core, and the lower plastic zone. Accordingly, the total moment is expressed as the sum of three double integrals, each accounting for the elastic strain contribution in its respective region. The variable ε^T denotes the total strain during loading, and ε^* represents the eigenstrain field, which equals the plastic strain and remains locked-in after unloading. The integral boundaries reflect the geometry of the rectangular section, with the constant width, 2 b, along the height, $2h$. This formulation sets the foundation for deriving

closed-form expressions for moment–curvature relations by evaluating each integral over its defined domain using the appropriate strain expressions.

$$M = E\int_{-h_e}^{h_e}\int_{-b}^{b}\left(\varepsilon^T-\varepsilon^*\right)ydxdy + E\int_{h_e}^{h}\int_{-b}^{b}\left(\varepsilon^T-\varepsilon^*\right)ydxdy + E\int_{-h}^{-h_e}\int_{-b}^{b}\left(\varepsilon^T-\varepsilon^*\right)ydxdy \tag{10}$$

2.2.1 Rectangular beam loaded

Equation 11 provides the explicit formulation of the internal bending moment in a rectangular beam during the loading phase, where the material undergoes elastic-perfectly plastic deformation. The derivation is based on the superposition of stress contributions from three distinct regions within the cross section that are the central elastic core and the symmetric plastic zones located at the top and bottom regions. In the elastic region, where no plastic deformation occurs, $|y| < h_e$, the total strain is entirely elastic and varies linearly with the vertical coordinate, y, contributing to the moment through the integral of $E\kappa y^2$. In the outer plastic regions ($h_e \le |y|$), the strain includes both elastic and plastic components, but since the plastic strain is not associated with stress during loading, the elastic part still dominates the stress calculation. However, to maintain accuracy, the plastic strain contribution, defined as $\varepsilon^*(y) = \kappa(|y| - h_e)$, is subtracted from the total strain in the stress expression. The resulting moment expression consists of five integrals that are three for the elastic contributions and two corrective integrals that subtract the moment effect due to the plastic strain in the outer zones. These integrals are evaluated across the appropriate limits of the beam height, with each term scaled by the beam width and the curvature. The formulation reflects the distribution of strain and stress during pure bending and prepares the groundwork for closed-form moment and curvature relations.

$$M = 2Eb\kappa\int_{-h_e}^{h_e} y^2dy + 2Eb\kappa\int_{h_e}^{h} y^2dy - 2Eb\kappa\int_{h_e}^{h}(y-h_e)ydy + 2Eb\kappa\int_{-h}^{-h_e} y^2dy - 2Eb\kappa\int_{-h}^{-h_e}(y+h_e)ydy \tag{11}$$

Equation 12b gives a simplified closed-form expression for the internal bending moment in a rectangular beam during loading by analytically evaluating the three integrals in Eq. 11 over the elastic core and the two outer plastic regions. The integration is performed region-by-region because the strain and eigenstrain (plastic strain) fields are piecewise that are within the central elastic core the eigenstrain is zero, so the stress is purely elastic and the moment contribution is governed by the familiar quadratic weighting with distance from the neutral axis. In the yielded outer regions, the total strain still varies linearly with the thickness coordinate, but only the elastic portion of that strain can generate stress and the remaining part is permanent plastic strain and is introduced as an eigenstrain. As a result, the moment contribution of each plastic region can be interpreted as an elastic-like contribution associated with the total strain field minus a corrective contribution that subtracts the stress-free eigenstrain component. Combining the three regional contributions produces a compact nonlinear moment–curvature relation that reflects the progressive growth of the plastic zones as loading increases.

$$M = \frac{4Eb\kappa}{3}h_e^3 + \frac{4Eb\kappa}{3}\left(h^3 - {h_e}^3\right) - \frac{2Eb\kappa}{3}\left(2h^3 - 3h^2h_e + {h_e}^3\right) \tag{12a}$$

$$M = \frac{2Eb\kappa h_e}{3}\left(3h^2 - {h_e}^2\right) \tag{12b}$$

A key point is that the elastic–plastic boundary position, h_e, is not an independent parameter. It is tied to the applied curvature through the yield condition at the boundary. Therefore, the limiting case of vanishing elastic core corresponds physically to increasing curvature while maintaining the yield condition, not to shrinking the elastic core at fixed curvature. Under the physically relevant fully plastic limit, the stress distribution approaches the yield stress over almost the entire cross section, in tension on one side and compression on the other, and the bending moment approaches a finite plastic limit rather than collapsing to zero. This interpretation resolves the apparent contradiction when one inspects the expression while holding curvature, κ, constant, and it clarifies how Eq. 12 captures the transition from elastic bending to partially and fully plastic bending, forming the basis for the subsequent springback and residual-stress analysis.

2.2.2 Rectangular beam unloaded

The mathematical formulation in Eq. 13 describes the internal moment in a rectangular beam during the unloading phase, following inelastic bending. In this state, the external bending moment, M, has been fully removed, and the remaining internal stresses arise solely due to the incompatibility introduced by the locked-in eigenstrain field. The total strain at any vertical position, y, now comprises the residual elastic strain and the permanent eigenstrain. The moment is therefore obtained by integrating this stress multiplied by the moment arm, y, across the beam's cross section. The expression is decomposed into five integrals where three representing the residual elastic contributions in the elastic core and the formerly plastified outer zones, and two compensating for the effect of the eigenstrain in the plastic regions. Specifically, the elastic terms involve $\kappa_r y$ as the strain, while the eigenstrain terms retain the same piecewise form as in the loading case. Importantly, the plastic strain remains fixed during unloading and is treated as an internal strain source that induces self-equilibrated residual stresses. Each integral is scaled by the beam width, $2b$, the elastic modulus, E, and the curvature, κ_r, which now represents the residual curvature after springback. This integral formulation lays the foundation for determining the residual stress state and permanent deformation geometry of the beam after unloading.

$$M = 2Eb\kappa_r \int_{-h_e}^{h_e} y^2 dy + 2Eb\kappa_r \int_{h_e}^{h} y^2 dy - 2Eb\kappa \int_{h_e}^{h} (y - h_e) y dy + 2Eb\kappa_r \int_{-h}^{-h_e} y^2 dy - 2Eb\kappa \int_{-h}^{-h_e} (y + h_e) y dy \tag{13}$$

Equation 14b provides the closed-form expression for the internal bending moment, M, in the unloaded rectangular beam, derived by analytically evaluating the integrals outlined in Eq. 13. The moment is expressed as a combination of two principal contributions that are the elastic recovery due to the residual curvature, κ_r, and the counteracting moment, M, induced by the locked-in eigenstrain field, which remains unchanged from the plastic strain developed during loading. The first term represents the elastic moment contribution integrated across the entire height of the beam, taking into account the residual curvature after unloading. The second term accounts for the internal moment generated by the eigenstrain field that drives the residual stress state. Since the beam is no longer externally loaded, these two effects must balance, and the net internal moment must be zero to satisfy equilibrium. By enforcing this zero-moment condition, the residual curvature is isolated in terms of the applied curvature, the yield strain, and the geometry of the cross section, particularly the extent of the plastified region. This relationship captures the essence of springback, quantifying the elastic recovery in curvature that occurs after removal of the applied bending moment, M, and highlights how the residual curvature depends nonlinearly on both the material response and the progression of plastic deformation through the cross section.

$$M = \frac{4Eb\kappa_r}{3} h_e^3 + \frac{4Eb\kappa_r}{3} \left(h^3 - {h_e}^3\right) - \frac{2Eb\kappa}{3} \left(2h^3 - 3h^2 h_e + {h_e}^3\right) = 0 \tag{14a}$$

$$M = \frac{4Eb\kappa_r}{3} h^3 - \frac{2Eb\kappa}{3} \left(2h^3 - 3h^2 h_e + {h_e}^3\right) = 0 \tag{14b}$$

Equation 15 presents the final closed-form expression for the residual curvature as a function of the applied curvature, the beam half-height, h, and the elastic-core height, h_e, which marks the boundary between the central elastic region and the plastified outer layers. This result follows from the moment equilibrium condition in Eq. 14 where after unloading, the bending moment associated with the residual elastic strain field, represented through the residual curvature, must exactly balance the self-equilibrated moment produced by the retained eigenstrain distribution. Equation 15 therefore expresses the residual curvature as being proportional to the curvature, multiplied by a nonlinear geometric factor that depends on the relative size of the elastic core. The structure of the expression reflects how both the elastic-core contribution and the plastic-zone contribution enter the equilibrium through thickness-weighted moment terms where the terms involving the elastic-core depth capture the progressive reduction of the elastic core and the corresponding increase in the retained eigenstrain, while the normalization by the full section height ensures a consistent scaling with cross section geometry. As plastic deformation penetrates deeper into the section as the elastic-core depth decreases, a larger portion of the total curvature is stored as eigenstrain and cannot be recovered elastically, so the recovered curvature increases and the residual curvature becomes a smaller fraction of the applied curvature, indicating greater springback. In the opposite limit, as the elastic-core height, h_e, approaches the beam half-height, h, plastic penetration

vanishes and the eigenstrain tends to zero and with the external moment removed, moment equilibrium then requires the residual stress resultants to vanish, which is satisfied by a vanishing residual curvature, κ_r. Thus, Eq. 15 predicts as the residual curvature goes to zero in the purely elastic limit, maximal recovery, while it predicts the residual curvature approaching the curvature when plasticity is extensive and elastic recovery is small. This closed-form relation provides a direct link between the elastic–plastic bending state during loading and the final unloaded beam shape, enabling practical prediction of residual curvature in bending-dominated forming and springback-sensitive design.

$$\kappa_r = \kappa \frac{2h^3 - 3h^2 h_e + {h_e}^3}{2h^3} \tag{15}$$

Equation 16 quantifies the strain relaxation, $\delta\varepsilon(y)$, across the total beam height, $2h$, following unloading, representing the difference between the elastic strain during loading and the residual elastic strain after springback. This quantity is essential for characterizing the redistribution of internal stresses once the external moment is removed. As derived, the strain relaxation is linearly proportional to the vertical coordinate, y, scaled by the difference between the applied, κ, and residual, κ_r, curvatures. By substituting the expression for the residual curvature from Eq. 15, the strain relaxation is reformulated explicitly in terms of the yield strain, the beam half-height, h, and the elastic-core height, h_e. The resulting expression reveals that the amount of elastic strain released during unloading is greatest at the outermost regions and diminishes linearly towards the neutral axis. This behaviour is consistent with the classical assumption of linear strain distribution in bending and highlights how the extent of plastic deformation influences the residual stress field. Importantly, the strain relaxation provides a direct measure of the self-equilibrating elastic response induced by the eigenstrain, offering insights into the residual stress gradients that persist within the beam after forming operations.

$$\delta\varepsilon(y) = (\kappa - \kappa_r)y = \left(\kappa - \kappa \frac{2h^3 - 3h^2 h_e + {h_e}^3}{2h^3}\right) y = \frac{\left(3h^2 - {h_e}^2\right)\varepsilon_y y}{2h^3} \tag{16}$$

2.3 Circular beam

Circular beams require the same eigenstrain logic as rectangular beams, but the sectional integration changes because the effective strip width varies with the vertical coordinate, y. This introduces the characteristic radial weighting from the circular area element, and it leads to closed-form expressions containing trigonometric terms that reflect the geometry of the remaining elastic core. The following derivation retains the same structure, moment from elastic strain minus eigenstrain corrections, while adapting the integrals to cylindrical geometry.

Equation 17 formulates the general expression for the internal bending moment, M, in a circular cross-sectional beam within the eigenstrain framework, explicitly incorporating the geometric weighting that is unique to cylindrical sections. Unlike the rectangular case, where the cross-sectional integration uses a constant width in Cartesian coordinates, the circular geometry requires accounting for the fact that the width of a horizontal strip varies with its vertical position. As a result, the moment is evaluated as an area integral of the axial stress multiplied by the moment arm, y, with the local strip area weighted by the corresponding chord length that is related with the radius, r, of the cross section. This introduces a characteristic square-root dependence in the through-thickness integration, reflecting the reduction of available material area as the strip approaches the outer boundary of the circle. Consistent with axisymmetry and elastic–perfectly plastic bending, the formulation is evaluated by decomposing the section into an elastic core and two outer plastic zones and in the plastic zones, the stress is obtained from the elastic response to the total strain after subtracting the eigenstrain contribution. This integral formulation serves as the starting point for the subsequent closed-form moment–curvature and springback expressions for circular beams and enables direct comparison with the rectangular case under the same constitutive assumptions.

$$M = E\int_{-h_e}^{h_e}\int_{-\left(r^2-y^2\right)^{0.5}}^{\left(r^2-y^2\right)^{0.5}} \left(\varepsilon^T - \varepsilon^*\right) y dx dy + E\int_{h_e}^{h}\int_{-\left(r^2-y^2\right)^{0.5}}^{\left(r^2-y^2\right)^{0.5}} \left(\varepsilon^T - \varepsilon^*\right) y dx dy + E\int_{-h}^{-h_e}\int_{-\left(r^2-y^2\right)^{0.5}}^{\left(r^2-y^2\right)^{0.5}} \left(\varepsilon^T - \varepsilon^*\right) y dx dy \tag{17}$$

2.3.1 Circular beam loaded

Equation 18 presents the detailed formulation of the internal bending moment, M, for a circular beam under loading, incorporating the effects of elastic–plastic deformation using the eigenstrain-based approach. The

beam is subjected to a pure bending moment that induces curvature, κ, resulting in a strain distribution that varies linearly with the vertical coordinate, y, across the cross section. To evaluate the internal moment, the stress, in the elastic region and adjusted for plastic strain in the plastic zones, is multiplied by the moment arm, y, and integrated over the entire cross-sectional area. Due to the circular geometry, the width of an infinitesimal horizontal strip at height, y, is $2\left(r^2 - y^2\right)^{0.5}$, which leads to a weighted integrand of the form $y^2\left(r^2 - y^2\right)^{0.5}$. The expression is separated into five integrals, corresponding to the upper plastic zone, the elastic core, and the lower plastic zone, with additional correction terms that subtract the contribution of the plastic strain. Specifically, the eigenstrain correction terms account for the reduction in stress-carrying capacity in the plastified regions by integrating $(y \pm h_e)y\left(r^2 - y^2\right)^{0.5}$ over the plastic domains. Each term is scaled by the elastic modulus, E, and the curvature, κ, and the integration bounds are chosen to reflect the geometry and symmetry of the circular cross section. This integral structure captures the composite nature of the stress distribution in the beam during loading and serves as the foundation for obtaining a closed-form moment–curvature relationship under inelastic bending conditions.

$$\begin{aligned} M =& 2E\kappa \int_{-h_e}^{h_e} y^2\left(r^2 - y^2\right)^{0.5} dy + 2E\kappa \int_{h_e}^{h} y^2\left(r^2 - y^2\right)^{0.5} dy - 2E\kappa \int_{h_e}^{h} (y - h_e)y\left(r^2 - y^2\right)^{0.5} dy \\ &+ 2E\kappa \int_{-h}^{-h_e} y^2\left(r^2 - y^2\right)^{0.5} dy - 2E\kappa \int_{-h}^{-h_e} (y + h_e)y\left(r^2 - y^2\right)^{0.5} dy \end{aligned} \tag{18}$$

Equation 19 presents a rearranged formulation of the internal bending moment, M, for a circular cross-sectional beam undergoing elastic–plastic bending, expressed using the eigenstrain-based approach. The derivation consolidates the five integrals from Eq. 18 into three principal terms by exploiting symmetry and combining regions with analogous mathematical structures. The first integral in Eq. 19 corresponds to the total elastic contribution from the entire cross section, incorporating both the elastic core and the plastified regions, and is represented by integrating $y^2\left(r^2 - y^2\right)^{0.5}$ over the total beam height, $2h$. The second and third terms introduce corrective contributions from the locked-in eigenstrain fields present in the plastified outer zones. These terms subtract the stress-free eigenstrain influence from the total moment expression, ensuring that only the recoverable elastic stress contributes to the internal bending resistance. Each of these correction terms is weighted by both the eigenstrain function and the radial area element, reflecting the geometrical dependence of stress distribution in cylindrical coordinates.

$$M = 2E\kappa \int_{-h}^{h} y^2\left(h^2 - y^2\right)^{0.5} dy - 2E\kappa \int_{h_e}^{h} (y - h_e)y\left(h^2 - y^2\right)^{0.5} dy - 2E\kappa \int_{-h}^{-h_e} (y + h_e)y\left(h^2 - y^2\right)^{0.5} dy \tag{19}$$

Equation 20b provides the closed-form analytical expression for the internal bending moment, M, of a circular cross-sectional beam subjected to inelastic bending, derived from the integral formulation of Eq. 19. The solution incorporates the contributions of both the elastic and plastically deformed regions using cylindrical geometry, where the radial weighting function naturally arises from the circular cross-sectional area element. The first term represents the full elastic contribution of the entire circular cross section assuming a linear strain distribution with curvature. The subsequent terms subtract the moment contributions due to the eigenstrain field, which corresponds to the locked-in plastic strain in the outer regions beyond $y \pm h_e$. These subtractions involve sinusoidal and polynomial terms that account for the geometry-specific distribution of plastic strain and its impact on bending resistance. The presence of $\sin^{-1}(h_e/h)$ reflects the angular extent of the elastic–plastic boundary in polar coordinates, while the remaining terms capture the volumetric influence of the plastified zones. The entire expression is scaled by the elastic modulus, E, the curvature, κ, and geometric factors involving the radius, r, and the elastic-core height, h_e, thereby linking the moment, M, directly to the progression of plastic deformation within the cross section. This closed-form result is critical for accurately predicting the nonlinear moment–curvature response of circular beams and provides a basis for evaluating residual stress and curvature in the subsequent unloading analysis.

$$M = \frac{E\kappa}{12}\left[3\pi h^4\right] - \frac{E\kappa}{12}\left[3\pi h^4 - 6h^4 \sin^{-1}\left(\frac{h_e}{h}\right) - \left(10h_e h^2 - 4h_e^3\right)\left(h^2 - {h_e}^2\right)^{0.5}\right] \tag{20a}$$

$$M = \frac{E\kappa}{12}\left[6h^4\sin^{-1}\left(\frac{h_e}{h}\right) + \left(10h_e h^2 - 4h_e^3\right)\left(h^2 - {h_e}^2\right)^{0.5}\right] \tag{20b}$$

2.3.2 Circular beam unloaded

Equation 21 presents the integral formulation of the internal bending moment for a circular cross-sectional beam, with a radius of r, in the unloaded state, following inelastic deformation. In this phase, the external bending moment has been fully removed, and the internal moment arises solely from the residual elastic stresses induced by the eigenstrain field, which represents the irreversible plastic strains retained within the material. The expression is composed of three integrals. The first term accounts for the elastic recovery associated with the residual curvature, integrating $y^2\left(r^2 - y^2\right)^{0.5}$ across the full cross section to capture the self-equilibrated internal moment arising from residual elastic strain. The second and third integrals represent the correction terms due to the eigenstrain field that remains in the plastified regions, $|y| > h_e$. These eigenstrain contributions, weighted by the product $(y \pm h_e)y\left(r^2 - y^2\right)^{0.5}$, reflect the locked-in plastic strains and their influence on internal moment redistribution. The integrals are carefully structured to capture the asymmetry introduced by the plastic zones while maintaining the overall balance of internal forces and moments. As no external loading exists in this state, the total internal moment must satisfy the equilibrium condition of zero moment, which provides the foundation for deriving the residual curvature and characterizing the springback behaviour of the beam. This integral framework links material response, plastic deformation, and geometric properties, enabling an exact analytical evaluation of residual bending effects in axisymmetric geometries.

$$M = 2E\kappa_r \int_{-h}^{h} y^2\left(h^2 - y^2\right)^{0.5} dy - 2E\kappa \int_{h_e}^{h} (y - h_e)y\left(h^2 - y^2\right)^{0.5} dy - 2E\kappa \int_{-h}^{-h_e} (y + h_e)y\left(h^2 - y^2\right)^{0.5} dy \tag{21}$$

Equation 22 provides the closed-form analytical expression for the internal bending moment in the unloaded circular beam, derived by explicitly evaluating the integrals defined in Eq. 21. The formulation reflects the mechanical equilibrium condition in the absence of external moments, where the internal moment generated by the residual elastic strain must be exactly balanced by the moment induced by the locked-in eigenstrain field. The first term represents the moment contribution from the residual curvature, κ_r, distributed over the entire circular cross section with radial weighting accounted for by the term $y^2\left(r^2 - y^2\right)^{0.5}$. The second term, which is subtracted, captures the internal moment due to the eigenstrain field preserved in the plastified regions. This eigenstrain-induced moment is expressed as a sum of trigonometric and polynomial terms involving the elastic-core height, h_e, the beam radius, r, and geometric parameters that describe the angular and volumetric extent of plastic deformation. Specifically, the $\sin^{-1}(h_e/h)$ term quantifies the angular reach of the elastic core in cylindrical coordinates, while the polynomial expressions involving the elastic-core height, h_e, and radius, r, model the nonuniform distribution of eigenstrain within the outer plastified zones. By setting the total moment to zero, this equation implicitly defines the residual curvature in terms of the initial curvature, κ, thereby establishing a direct link between the imposed inelastic deformation during loading and the elastic recovery upon unloading. This equilibrium-based formulation is essential for predicting springback and residual stress fields in circular structural components subjected to plastic bending.

$$M = \frac{E\kappa_r}{12}\left[3\pi h^4\right] - \frac{E\kappa}{12}\left[3\pi h^4 - 6h^4\sin^{-1}\left(\frac{h_e}{h}\right) - \left(10h_e h^2 - 4h_e^3\right)\left(h^2 - {h_e}^2\right)^{0.5}\right] = 0 \tag{22}$$

Equation 23 presents the closed-form expression for the residual curvature, κ_r, of a circular cross-sectional beam after unloading, expressed in terms of the initial curvature, κ, the beam radius, and the elastic-core height, h_e. This result is obtained by solving the equilibrium condition established in Eq. 22, where the internal moment due to residual elastic strain must exactly counterbalance the moment generated by the locked-in eigenstrain field. The numerator of Eq. 23 encapsulates the contribution of the plastified zones through a combination of trigonometric and algebraic terms where the $\sin^{-1}(h_e/h)$ term accounts for the angular span of the remaining elastic core, while the remaining polynomial terms quantify the volumetric effect of the plastically deformed outer regions. Specifically, the expressions involving $10h_e h^2$ and $4h_e^3$ reflect the geometric amplification of the eigenstrain effect as plastic deformation progresses further from the neutral axis. The entire numerator is scaled by the initial curvature, κ, indicating that residual curvature, κ_r, is fundamentally driven by the

original bending deformation. The denominator, $3\pi h^4$, corresponds to the fully elastic flexural rigidity of the circular cross section and serves to normalize the expression. As the plastified region expands as the elastic-core height, h_e, decreases, the numerator increases in magnitude, resulting in a greater discrepancy between the initial curvature and the residual curvature, which corresponds to increased springback. Conversely, in the purely elastic limit, the eigenstrain terms vanish and the residual curvature tends to zero, indicating full recovery upon unloading. Thus, Eq. 23 offers a physically meaningful and geometrically precise prediction of residual curvature in inelastically bent circular beams.

$$\kappa_r = \kappa \frac{3\pi h^4 - 6h^4 \sin^{-1}\left(\frac{h_e}{h}\right) - \left(10h_e h^2 - 4h_e^3\right)\left(h^2 - {h_e}^2\right)^{0.5}}{3\pi h^4} \tag{23}$$

Equation 24 provides the expression for the strain relaxation across the height, $\delta\varepsilon(y)$, of a circular cross-sectional beam following unloading, quantifying the change in elastic strain resulting from the release of the external bending moment. This formulation directly follows from Eq. 9 and builds upon the previously derived expression for the residual curvature, κ_r, in Eq. 23. Substituting the residual curvature into the relaxation formula, Eq. 24 expresses the strain relaxation explicitly in terms of the initial curvature, the yield strain, the beam radius, r, and the elastic-core height, h_e. The numerator encapsulates the effect of inelastic deformation through the combination of a sinusoidal term, $\sin^{-1}(h_e/h)$, and polynomial terms in the elastic-core height, h_e, and the beam half-height, h, reflecting the spatial and volumetric influence of the plastic zones. These terms together describe how the locked-in eigenstrain field reduces the residual elastic strain, especially in regions farther from the neutral axis. The entire expression is scaled by the coordinate, y, preserving the linear variation of strain through the height of the beam, consistent with the assumptions of classical beam theory. The denominator normalizes the strain relaxation by the beam's elastic flexural stiffness and the size of the elastic core. Overall, Eq. 24 enables a detailed characterization of the residual elastic strain field, which is critical for predicting self-equilibrated stress distributions and understanding how geometric and material factors influence springback and residual stress gradients in axisymmetric components.

$$\delta\varepsilon(y) = (\kappa - \kappa_r)y = \frac{\left[6h^4 \sin^{-1}\left(\frac{h_e}{h}\right) + \left(10h_e h^2 - 4h_e^3\right)\left(h^2 - {h_e}^2\right)^{0.5}\right]\varepsilon_y y}{3\pi h^4 h_e} \tag{24}$$

2.4 I-beam

I-beams exhibit strong geometric non-uniformity that is most bending stiffness resides in the flanges, while the web carries relatively less moment but couples the flanges and controls the section depth. This geometry requires a region-wise treatment of yielding because the plastified zones typically develop in the flanges first and evolve differently from the web. The eigenstrain approach remains the same as before, plastic strain generated during loading is retained as eigenstrain after unloading, but the sectional integrals must be written as a sum over web and flange subdomains.

Equation 25 presents the general integral formulation of the internal bending moment M for an I-beam cross section undergoing inelastic deformation, based on the eigenstrain framework. Due to the complex geometry of the I-beam, the cross section is partitioned into five distinct regions that are the central web, the upper and lower flanges, and their respective plastified zones. The bending moment is computed by integrating the product of stress and moment arm, y, over the entire cross-sectional area, with stress determined through Hooke's law. Each integral in Eq. 25 corresponds to a different region of the cross section, accounting for both the elastic contribution and the locked-in plastic strain through eigenstrain. The integrals are expressed in terms of Cartesian coordinates, x and y, with integration limits tailored to the geometry of the I-beam flanges and web. In the flanges, where the width is greater and bending stresses dominate, the eigenstrain plays a significant role in generating residual moment. In the web region, the contribution is narrower but more centrally located. This decomposition enables precise treatment of the asymmetric plastic deformation typically observed in I-beams under bending. Equation 25 thus establishes the foundational moment expression necessary for evaluating both the loading and unloading behaviour of the I-beam by incorporating geometric segmentation and inelastic strain localization within a unified eigenstrain-based framework.

$$M = E\int_{-w}^{w}\int_{-b}^{b}\left(\varepsilon^T - \varepsilon^*\right)dxdy + E\int_{w}^{h_e}\int_{-a}^{a}\left(\varepsilon^T - \varepsilon^*\right)dxdy$$

$$+ E \int_{-h_e}^{-w} \int_{-a}^{a} \left(\varepsilon^T - \varepsilon^*\right) dxdy + E \int_{h_e}^{h} \int_{-a}^{a} \left(\varepsilon^T - \varepsilon^*\right) dxdy + E \int_{-h}^{-h_e} \int_{-a}^{a} \left(\varepsilon^T - \varepsilon^*\right) dxdy + \tag{25}$$

2.4.1 I-beam loaded

Equation 26 provides the expanded formulation of the internal bending moment for an I-beam during the loading phase, incorporating the effects of elastic–plastic deformation within the eigenstrain framework. The expression decomposes the total moment into contributions from both the web and flange regions, each of which may contain elastic and plastified zones depending on the applied curvature. The first term accounts for the elastic moment contribution from the central web, integrating $E\kappa y^2$ across the web height and thickness. The subsequent four terms represent the contributions from the upper and lower flanges that are the second and third integrals capture the elastic response of the flange material, while the fourth and fifth integrals introduce correction terms for the eigenstrain field in the plastified outer regions. These correction terms subtract the non-recoverable plastic strain (eigenstrain) from the total strain to isolate the stress-producing elastic component. The notation 2 $Ea\kappa$ reflects the dependence on the elastic modulus, the flange width, 2 a, and the applied curvature, κ, while integration is carried out over the corresponding limits in the vertical coordinate, y, ensuring accurate modelling of both the symmetric elastic core and plastified boundary zones. This formulation captures the nonuniform stress and strain distribution characteristic of I-beam geometries, particularly where flanges dominate the bending resistance. The explicit inclusion of eigenstrain corrections ensures that the moment calculation properly accounts for irreversible inelastic deformation during loading, laying the groundwork for obtaining a closed-form moment–curvature relationship.

$$\begin{aligned} M = {} & 2Eb\kappa \int_{-w}^{w} y^2 dx + 2Ea\kappa \int_{w}^{h_e} y^2 dy + 2Ea\kappa \int_{-h_e}^{-w} y^2 dy + 2Ea\kappa \int_{h_e}^{h} y^2 dy \\ & - 2Ea\kappa \int_{h_e}^{h} (y - h_e) y dy + 2Ea\kappa \int_{-h}^{-h_e} y^2 dy - 2Ea\kappa \int_{-h}^{-h_e} (y + h_e) y dy \end{aligned} \tag{26}$$

Equation 27 presents the closed-form analytical expression for the internal bending moment, M, in an I-beam subjected to inelastic bending under an applied curvature, κ, derived by explicitly evaluating the integrals in Eq. 26. The formulation incorporates the contributions from both the web and flanges, while accounting for the development of plastified regions and the associated eigenstrain field. The first three terms represent the elastic contributions from the central web, the partially plastified flange region, and the fully plastified outer flange region. These terms scale with the elastic modulus, the beam width, either web width, 2 b, or flange width, 2 a, and the applied curvature, κ, and are each weighted by their respective geometric parameters through cubic powers of height. The final term introduces the correction due to the eigenstrain, which subtracts the bending moment contribution of the plastified, non-recoverable, strain field. This correction term involves a combination of linear and cubic functions of the elastic-core height, h_e, and total flange height, 2 h, and captures the reduction in elastic restoring moment due to permanent deformation. The simplification of the full expression yields the compact form, reflecting the nonlinear evolution of the moment–curvature relationship as plasticity progresses. This final form demonstrates how the inelastic response of the I-beam is governed not only by the applied curvature but also by the extent of plastic penetration into the cross section, offering a rigorous foundation for predicting structural behaviour during the loading phase.

$$M = \frac{4Eb\kappa}{3} w^3 \frac{4Ea\kappa}{3} + \left({h_e}^3 - w^3\right) + \frac{4Ea\kappa}{3}\left(h^3 - {h_e}^3\right) - \frac{2Ea\kappa}{3}\left(2h^3 - 3h^2 h_e + {h_e}^3\right) \tag{27a}$$

$$M = \frac{4Eb\kappa}{3} w^3 + \frac{2Ea\kappa}{3}\left(3h^2 h_e - {h_e}^3 - 2w^3\right) \tag{27b}$$

2.4.2 I-beam unloaded

Equation 28 defines the total internal bending moment, M, in an I-beam cross section during the unloading phase, where the externally applied moment has been removed and the stress state arises solely from the

residual elastic response to the locked-in eigenstrain field. The formulation is based on integrating the product of residual stress and the moment arm, y, over the entire cross-sectional area, which is subdivided into distinct geometric regions corresponding to the web and flanges. Specifically, the I-section is partitioned into the central web region and the top and bottom flanges, each contributing independently to the total internal moment. The residual elastic strain is associated with the residual curvature, κ_r, while the eigenstrain, originating from the permanent plastic deformation developed during loading, remains unchanged. The total moment is expressed as the sum of multiple integrals that are three corresponding to the elastic contributions from the web and both flanges, and two additional integrals representing the counteracting moment generated by the eigenstrain in the plastified regions of the flanges. The subtraction of these eigenstrain terms reflects the reduction in internal elastic stress due to irreversible plastic flow. The expression retains geometric parameters such as the web height, 2 w, the total cross-sectional height, 2 h, and flange width, 2 a, and includes the elastic modulus, E, and beam width, 2 b. This comprehensive integral structure captures the complex interaction between geometry, material behaviour, and residual curvature, providing the groundwork for deriving a closed-form expression for springback in I-beam structures.

$$M = 2Ea\kappa_r \int_{-w}^{w} y^2 dy + 2Ea\kappa \int_{w}^{h_e} y^2 dy + 2Ea\kappa_r \int_{-h_e}^{w} y^2 dy + 2Ea\kappa_r \int_{h_e}^{h} y^2 dy$$
$$- 2Ea\kappa_r \int_{h_e}^{h} (y - h_e) y dy + 2Ea\kappa_r \int_{h}^{-h_e} y^2 dy - 2Ea\kappa \int_{-h}^{-h_e} (y + h_e) y dy \tag{28}$$

Equation 29b presents the simplified closed-form expression for the internal bending moment, M, in the unloaded I-beam, derived by analytically evaluating the integrals introduced in Eq. 28 and enforcing the condition of static equilibrium. In the absence of an external moment, the internal moment generated by the residual elastic strain must be exactly balanced by the opposing moment produced by the locked-in eigenstrain field. The first term represents the total elastic moment associated with the residual curvature, κ_r, integrated across the composite cross section of the web and flanges. This term aggregates the elastic contributions of the I-beam geometry into a single, curvature-dependent moment expression. The second term corresponds to the internal moment resulting from the eigenstrain distribution developed during loading, expressed in terms of the initial curvature, κ, total beam height, 2 h, and the elastic-core height, h_e. By setting the net internal moment to zero, this equation establishes a balance between the elastic recovery and the permanent inelastic deformation, enabling a direct solution for the residual curvature. This formulation encapsulates the key physical mechanisms governing springback in I-beams and provides a basis for quantifying residual deformation in terms of material properties and cross-sectional geometry.

$$M = \frac{4Eb\kappa_r}{3} w^3 \frac{4Ea\kappa_r}{3} + \left(h_e^3 - w^3\right) + \frac{4Ea\kappa_r}{3}\left(h^3 - h_e^3\right) - \frac{2Ea\kappa}{3}\left(2h^3 - 3h^2 h_e + h_e^3\right) = 0 \tag{29a}$$

$$M = \frac{4Eb\kappa_r}{3} w^3 + \frac{4Ea\kappa_r}{3}\left(h^3 - w^3\right) - \frac{2Ea\kappa}{3}\left(2h^3 - 3h^2 h_e + h_e^3\right) = 0 \tag{29b}$$

Equation 30 provides the closed-form solution for the residual curvature in an I-beam following unloading, expressed as a function of the initially applied curvature, κ, the total cross-sectional height and the elastic-core height, h_e. This expression is derived directly from the moment equilibrium condition established in Eq. 29, wherein the moment generated by the residual elastic strain counterbalances the moment induced by the locked-in eigenstrain. The numerator captures the nonlinear influence of the plastically deformed regions on the residual curvature. As the plastic region expands as the elastic-core height, h_e, decreases, the eigenstrain-induced moment becomes more dominant, resulting in a greater reduction in residual curvature relative to the initial curvature. Conversely, when the elastic-core height, h_e, approaches the beam half-height, h, indicating minimal plastic deformation, the numerator tends towards the total cross-sectional height, h, and the residual curvature, κ_r, asymptotically approaches the applied curvature, indicating negligible springback. The total cross-sectional height in the denominator, serves as a geometric scaling factor, ensuring the expression remains dimensionally consistent. This relationship encapsulates the influence of inelastic deformation on residual shape retention in I-beams and highlights the sensitivity of springback behaviour to both the extent

Table 1 Geometric and material parameters used in the analytical eigenstrain formulations for rectangular, circular, and I-beam cross sections

Parameter	Rectangular beam	Circular beam	I-beam
E	100 GPa	100 GPa	100 GPa
h	1.0 m	1.0 m	1.0 m
w	–	–	0.75 m
a	–	–	0.5 m
b	0.125 m	–	0.125 m
h_e	0.8 m	0.8 m	0.8 m

of plasticity and the overall section geometry, making it a critical tool for predictive modelling in forming and structural applications.

$$\kappa_r = a\kappa \frac{2h^3 - 3h^2 h_e + {h_e}^3}{2\left[bw^3 + a\left(h^3 - w^3\right)\right]} \tag{30}$$

Equation 31 expresses the strain relaxation in the I-beam cross section as a function of vertical position y, quantifying the amount of elastic strain released during unloading due to the difference between the applied and residual curvatures, where κ is the curvature under the applied moment and residual curvature, κ_r, is the residual curvature after unloading. By substituting the expression for residual curvature from Eq. 30, the strain relaxation is reformulated in terms of beam geometry and material response. Specifically, it incorporates the yield strain and depends on the relative size of the plastified region. This reflects the nonlinear relationship between the elastic-core height, h_e, and the extent of elastic recovery. The expression shows that strain relaxation increases linearly with the distance from the neutral axis and reaches its maximum at the outermost fibres. As plastic deformation deepens with smaller the elastic-core height, h_e, the magnitude of strain relaxation increases, indicating greater internal stress redistribution. This formulation is crucial for understanding the development of residual stresses in I-beam structures after bending, and it provides valuable insight into how cross-sectional geometry and plastic zone progression affect the final strain state, which is essential for accurate predictions of springback and long-term structural performance.

$$\delta\varepsilon(y) = (\kappa - \kappa_r)y = \left(1 - a\frac{2h^3 - 3h^2 h_e + {h_e}^3}{2\left[bw^3 + a\left(h^3 - w^3\right)\right]}\right)\frac{\varepsilon_y y}{h_e} \tag{31}$$

3 Results and discussion

To evaluate and compare the inelastic bending responses of different beam geometries, the analytical formulations developed in the preceding sections were implemented using MATLAB. This section demonstrates how the same eigenstrain-driven workflow yields consistent moment–curvature relations, residual curvature after unloading, and associated residual elastic strain (strain relaxation) fields for each geometry within a single analytical framework. The solutions capture the evolution of total, plastic, and elastic strain distributions during and after bending, as well as the resulting residual curvature and moment–curvature behaviour. Key parameters used in the models are listed in Table 1. The analysis focuses on rectangular, circular, and I-beam cross sections subjected to pure bending, and includes computation of strain profiles, residual stress characteristics, springback magnitudes, and nonlinear moment–curvature responses. The results provide insight into how geometric factors influence plastic zone development, elastic recovery, and load-bearing performance in elastoplastic bending regimes, while also providing a transparent basis for cross-checking the closed-form expressions against independent classical benchmarks.

The top-left plot in Fig. 3 illustrates the through-thickness distribution of total, plastic, and elastic axial strains in a circular beam during the loading phase under pure bending. The total strain profile exhibits the expected linear variation with respect to the vertical position within the cross section, consistent with classical Euler–Bernoulli beam theory. Plastic strain localizes symmetrically at the outermost regions of the beam, forming distinct plastified zones where the strain exceeds the yield strain. Within these regions, the plastic strain increases linearly with distance from the neutral axis, as described by the piecewise definition of the eigenstrain field. In contrast, the central core of the cross section remains purely elastic, where the total strain is fully recoverable and coincides with the elastic strain. The transition between the elastic and plastic zones is

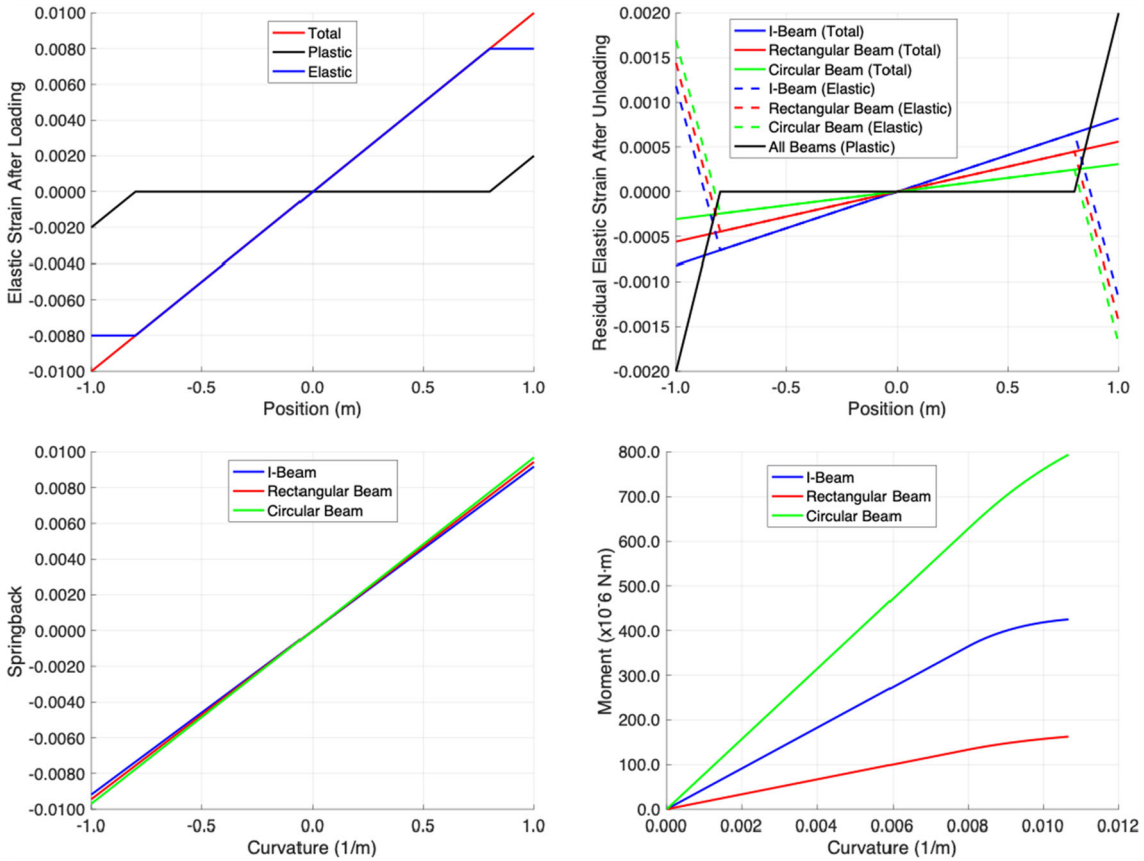

Fig. 3 Analytical results for rectangular, circular, and I-beam cross sections modelled with elastic–perfectly plastic behaviour. (Top left) Decomposition of total, plastic, and elastic strains through the thickness of a circular beam during loading. (Top right) Residual elastic strain distributions following unloading. (Bottom left) Strain relaxation profiles across the beam height corresponding to elastic recovery. (Bottom right) Comparison of nonlinear moment–curvature responses for the three geometries

marked by the elastic limit beyond which inelastic deformation becomes dominant. This behaviour reflects the influence of the circular geometry on the distribution of bending-induced strain, where the curvature-induced stress and strain vary smoothly across the radius, and highlights how plastic deformation concentrates near the outer regions under bending-dominated loading. The results confirm the analytical assumption that plastic strain evolves in the outer regions during loading and can subsequently be treated as an eigenstrain field responsible for the formation of residual stresses upon unloading.

The top-right plot in Fig. 3 presents the residual elastic strain distributions across the cross sections of I-beam, rectangular, and circular geometries following unloading, highlighting the self-equilibrated strain fields that result from locked-in eigenstrains. Notably, the I-beam exhibits the lowest peak residual elastic strain magnitude among the three geometries, followed by the rectangular beam, while the circular beam demonstrates the highest residual strain levels. This ordering is primarily attributed to the geometric stiffness distribution and the extent of plastification within each cross section. Despite exhibiting the largest curvature after unloading, the I-beam's wider flanges and deeper web create a highly efficient distribution of stiffness, enabling it to recover more of its elastic deformation and thus retain lower residual strain. In contrast, the circular beam, despite having the smallest residual curvature, shows the highest residual elastic strain, owing to the radial distribution of plastic zones and the limited geometric constraint in the outer regions, where plastic deformation is most pronounced. The rectangular beam presents intermediate behaviour both in terms of curvature and residual strain, balancing between the stiffness localization seen in the I-beam and the uniformity of the circular cross section. These results illustrate the complex interplay between geometry, elastic recovery, and plastic strain retention, and emphasize how cross-sectional shape fundamentally influences the magnitude and distribution of residual strains in bending-dominated deformation processes.

The bottom-left plot in Fig. 3 depicts the strain relaxation profiles across the beam height for the circular, rectangular, and I-beam cross sections, offering a direct representation of springback behaviour following unloading. Springback is quantified here as the difference between the elastic strain during loading and the residual elastic strain after unloading, and it varies linearly with vertical position, consistent with the theoretical formulation of springback given at Eq. 9. Among the three geometries, the circular beam exhibits the highest springback magnitude, reflecting a greater release of stored elastic strain energy upon unloading. This pronounced springback is a result of the circular cross section's symmetric stress distribution and its limited geometric stiffness at the outer regions, which allows greater plastic deformation during loading and subsequently larger elastic recovery. In contrast, the I-beam shows the lowest springback magnitude, despite having the highest residual curvature, due to its optimized structural geometry with flanges and web that effectively constrain deformation and limit elastic strain accumulation. The rectangular beam once again demonstrates intermediate behaviour, with moderate springback levels governed by its uniform stiffness and more constrained plasticization relative to the circular beam. These findings underscore the importance of cross-sectional geometry in controlling elastic recovery and have practical implications for the prediction and compensation of springback in metal forming and structural design applications.

The bottom-right plot in Fig. 3 illustrates the moment–curvature responses for the I-beam, rectangular beam, and circular beam geometries under increasing inelastic bending. As shown, the circular beam exhibits the highest bending moment for a given curvature, followed by the I-beam, while the rectangular beam demonstrates the lowest moment capacity across the range. This variation is fundamentally governed by the geometric distribution of material relative to the neutral axis, which directly affects the flexural rigidity of each cross section. The circular beam, possessing a continuous and symmetric geometry with material distributed uniformly about the centre, maximizes the second moment of area, thereby enabling it to sustain higher bending moments before significant plastic deformation occurs. In contrast, the rectangular beam, while geometrically simpler, has a comparatively smaller cross-sectional area and a less efficient distribution of material in resisting bending, particularly in the absence of flanges or structural reinforcements. The I-beam, although featuring localized stiffness enhancements through its flanges and web, does not achieve the same total cross-sectional area or radial material distribution as the circular section. However, its tailored geometry allows for high stiffness-to-weight performance and improved springback control, as shown in the other plots. The observed differences in moment–curvature behaviour not only reflect the underlying geometric and material assumptions of the eigenstrain-based model, but also emphasize the practical implications for structural design, where maximizing moment capacity, minimizing weight, or controlling residual deformation each necessitate specific cross-sectional strategies.

Figure 4 presents a parametric sensitivity study of springback with respect to the yield strain, showing the predicted residual curvature as a function of yield strain for three canonical cross sections, that are rectangular, circular, and I-shaped, at several fixed applied curvatures κ. For a given imposed curvature, increasing yield strain raises the elastic limit and reduces the extent of plasticity, so the permanent curvature decreases and approaches zero as the response becomes fully elastic. Conversely, decreasing yield strain promotes deeper yielding, leading to larger retained curvature after unloading. The curves also demonstrate the coupled influence of geometry and loading level. At higher applied curvature the residual curvature is larger for the same yield strain, reflecting the increased plastic penetration required to sustain the imposed bending. Differences among the three geometries arise from their sectional stiffness distribution, which governs how plastic zones develop and how much elastic recovery is available during unloading; for the I-section, the trends are strongly influenced by the dominance of the flanges in bending resistance, while the circular section exhibits a comparatively smoother sensitivity due to its continuously varying width. Overall, the figure provides a compact visualization of how yield strength and cross-sectional geometry jointly control springback magnitude under consistent beam-theory assumptions.

4 Verification against an independent classical benchmark

To verify the closed-form solutions based on eigenstrain, an independent benchmark was generated using classical beam plasticity under the same assumptions as this paper are Euler–Bernoulli kinematics, small strain, isotropic linear elasticity, elastic–perfectly plastic behaviour, pure bending, and symmetric cross sections [61, 88–92]. Verification is performed through an independent analytical/numerical benchmark under identical assumptions; direct comparison with finite-element or experimental springback datasets is an important next step but is outside the present closed-form baseline scope.

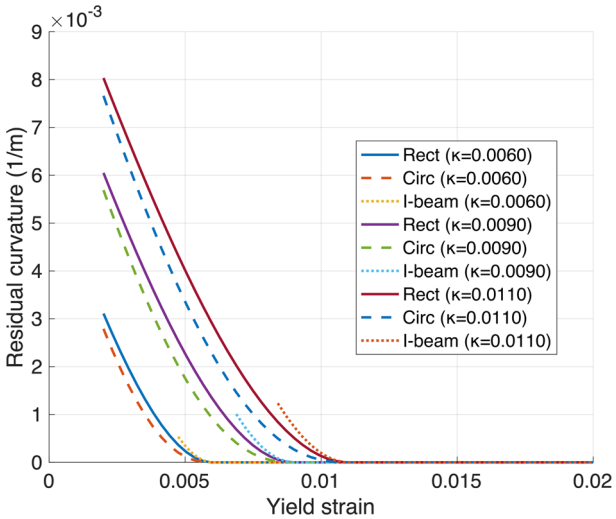

Fig. 4 Parametric sensitivity of springback to yield strain for three beam cross sections, that are rectangular, circular, and I-shaped, under pure bending. The residual curvature after unloading is plotted as a function of the applied curvature for several yield-strain values, with all other material and geometric parameters held constant. The curves illustrate how increasing yield strain delays the onset of plasticity, increases the elastic-core height, h_e, and therefore increases springback at a given applied curvature, while lower yield strain promotes earlier yielding and reduces springback

Importantly, the benchmark procedure is independent of the eigenstrain derivation and it constructs the standard piecewise elastic–perfectly plastic stress field during loading from classical perfectly plastic bending theory, computes the sectional bending moment by direct integration, and then applies elastic unloading through the sectional elastic stiffness to obtain curvature recovery and residual curvature. No eigenstrain decomposition is used in the benchmark and agreement therefore provides an external consistency check rather than a circular derivation. For a prescribed applied curvature, the elastic-core height, h_e, was obtained from the yield condition as the minimum of the beam half-height, h, or the radius, r, for a circular section, and the yield strain divided by the applied curvature [88–92]. The loading stress distribution was then constructed using standard perfectly plastic bending theory where the stress varies linearly with distance from the neutral axis within the elastic core, while the outer regions are fully yielded with constant magnitude equal to the yield stress, taking the sign according to tension or compression [88–92].

The sectional bending moment was computed by numerically integrating the classical stress resultant over the cross-sectional area, implemented as a one-dimensional integration over the thickness coordinate using the appropriate strip-width function; specifically, the strip width is constant for the rectangular section, equals twice the square root of radius squared minus the thickness-coordinate squared for the circular section, and is defined piecewise for the I-section to account for the web and flanges [88–92]. Finally, springback was obtained from purely elastic unloading by removing the applied moment produces an elastic curvature recovery equal to the applied moment divided by the elastic bending stiffness, so the residual curvature equals the applied curvature minus this recovery [90–93].

Figure 5 shows that the benchmark and closed-form curves are essentially indistinguishable for both the moment–curvature response and the springback curvature across the full curvature range investigated (elastic regime and post-yield regime) for all three geometries, consistent with classical expectations for elastic–perfectly plastic bending and elastic unloading [88–93]. This visual overlap is quantified by the relative-error plot, where errors remain extremely small, on the order of 10^{-4} or below over most of the range, indicating that differences are dominated by numerical quadrature/discretization in the benchmark integration rather than any systematic bias in the closed-form expressions. The I-beam case exhibits the largest deviation at higher curvature, which is expected because the width function is discontinuous at the web–flange junction and therefore converges more slowly under simple strip integration; increasing the integration resolution reduces this residual discrepancy. The residual stress profile cross-check for the rectangular section also shows near-perfect overlap between the stress reconstructed from the closed-form residual curvature and that obtained using the benchmark curvature, confirming that the agreement extends beyond scalar outputs to the full residual-field prediction. Overall, these cross-checks provide strong verification that the closed-form

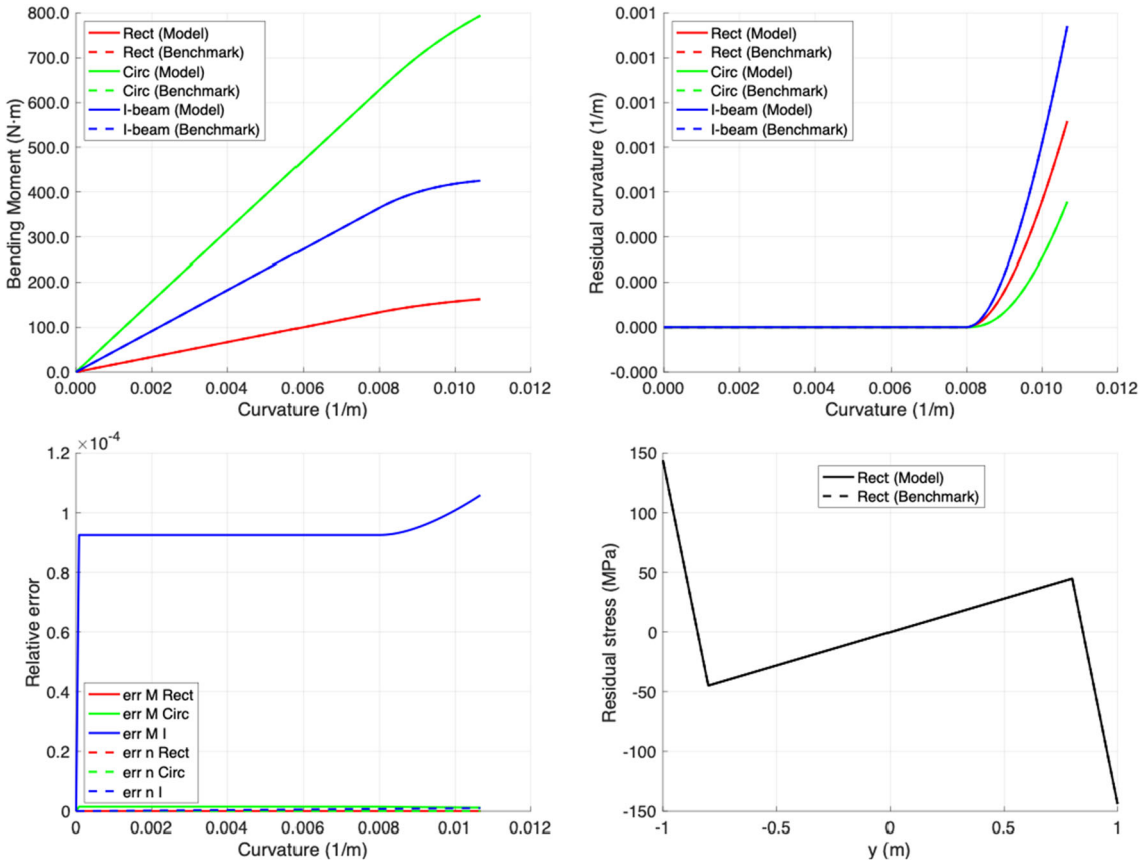

Fig. 5 Verification of the closed-form eigenstrain model against the independent classical elastoplastic benchmark. (Top left) Bending moment–curvature response for rectangular, circular, and I-shaped sections. (Top right) Residual curvature after unloading (springback) versus applied curvature. (Bottom left) Relative errors in bending moment and residual curvature calculations. (Bottom right) Comparison of residual stress distributions across the rectangular section height after unloading

eigenstrain-based formulas reproduce the classical elastoplastic bending and elastic-unloading predictions under the same modelling assumptions [88–93].

5 Conclusions

This work reformulates the classical springback of inelastically bent prismatic beams within the eigenstrain framework by treating the plastic strain accumulated during loading as a retained inelastic strain field that drives the residual elastic response after unloading. Within Euler–Bernoulli kinematics and elastic–perfectly plastic behaviour, closed-form expressions are obtained for rectangular, circular, and I-shaped cross sections, providing a unified analytical route to moment–curvature relations during loading and to residual curvature, strain relaxation, and self-equilibrated residual stress distributions after unloading. Comparative results highlight how cross-sectional geometry controls plastic-zone development, elastic recovery, and residual-field magnitudes under pure bending.

The closed-form predictions are verified against an independent classical beam-plasticity benchmark. Excellent agreement across the elastic and post-yield regimes confirms that the eigenstrain formulation reproduces classical springback behaviour while making the residual-stress interpretation explicit and reusable.

The present results are intentionally restricted to prismatic beams in pure bending, small-strain kinematics, and elastic–perfectly plastic response to preserve compact closed-form evaluation. More general constitutive effects, such as hardening, anisotropy, rate dependence, can be incorporated through more general eigenstrain inputs obtained from incremental modelling, numerical simulation, or inverse identification, although closed-form evaluation may then be replaced by numerical quadrature. In this sense, the study provides a verified analytical baseline connecting classical springback with eigenstrain-based residual-stress mechanics

for geometry comparisons and future extensions. Future work should incorporate hardening laws to generate more realistic eigenstrain distributions during loading and compare the resulting springback and residual-stress predictions directly with finite-element springback simulations and available experimental bending/springback datasets.

Author contributions Fatih Uzun: Conceptualization, Methodology, Software, Validation, Formal analysis, Investigation, Resources, Data curation, Writing—Original Draft, Writing—Review & Editing, Visualization; Alexander M Korsunsky: Supervising, Conceptualization, Methodology, Project administration, Funding acquisition.

Data availability The MATLAB scripts used to implement the eigenstrain-based closed-form models and perform the analysis presented in this study are available in the publicly accessible data repository that can be accessed at https://doi.org/10.17632/z7jpdhbrj2.2.

Declarations

Conflict of interest The authors declare no conflict interest.

References

1. Tabatabaeian, A., Ghasemi, A.R., Shokrieh, M.M., Marzbanrad, B., Baraheni, M., Fotouhi, M.: Residual stress in engineering materials: a review. Adv. Eng. Mater. **24**, 1–28 (2022). https://doi.org/10.1002/adem.202100786
2. Guo, J., Fu, H., Pan, B., Kang, R.: Recent progress of residual stress measurement methods: a review. Chin. J. Aeronaut. **34**, 54–78 (2021). https://doi.org/10.1016/j.cja.2019.10.010
3. Franceschi, A., Stahl, J., Kock, C., Selbmann, R., Ortmann-Ishkina, S., Jobst, A., Merklein, M., Kuhfuß, B., Bergmann, M., Behrens, B.A., Volk, W., Groche, P.: Strategies for residual stress adjustment in bulk metal forming. Arch. Appl. Mech. **91**, 3557–3577 (2021). https://doi.org/10.1007/S00419-021-01903-7
4. McMeeking, R.M., Lee, E.H.: The generation of residual stresses in metal-forming processes. In: Residual stress and stress relaxation, pp. 315–329. Springer US, Boston, MA (1982)
5. Abvabi, A., Rolfe, B., Hodgson, P.D., Weiss, M.: The influence of residual stress on a roll forming process. Int. J. Mech. Sci. **101–102**, 124–136 (2015). https://doi.org/10.1016/j.ijmecsci.2015.08.004
6. Uzun, F., Bilge, A.N.: Ultrasonic investigation of the effect of carbon content in carbon steels on bulk residual stress. J. Nondestr. Eval. **34**, 11 (2015). https://doi.org/10.1007/s10921-015-0284-x
7. Uzun, F., Bilge, A.N.: Immersion ultrasonic technique for investigation of total welding residual stress. Procedia Eng. **10**, 3098–3103 (2011). https://doi.org/10.1016/j.proeng.2011.04.513
8. Chen, J., Salvati, E., Uzun, F., Papadaki, C., Wang, Z., Everaerts, J., Korsunsky, A.M.: An experimental and numerical analysis of residual stresses in a TIG weldment of a single crystal nickel-base superalloy. J. Manuf. Process. **53**, 190–200 (2020). https://doi.org/10.1016/j.jmapro.2020.02.007
9. Xiong, Q., Qu, Y., Robin, V., Smith, M.C.: Residual stress assessment for dissimilar metal welds in nuclear power plant. Int. J. Press. Vessels Pip. **206**, 105018 (2023). https://doi.org/10.1016/j.ijpvp.2023.105018
10. Akrivos, V., Muransky, O., Depradeux, L., Smith, M.C., Vasileiou, A., Deaconu, V., Kapadia, P.: On the accurate prediction of residual stress in a three-pass slot nickel-base repair weld by numerical simulations. J. Manuf. Mater. Process. (2022). https://doi.org/10.3390/jmmp6030061
11. Akrivos, V., Wimpory, R.C., Hofmann, M., Stewart, B., Muransky, O., Smith, M.C., Bouchard, J.: Neutron diffraction measurements of weld residual stresses in three-pass slot weld (Alloy 600/82) and assessment of the measurement uncertainty. J. Appl. Crystallogr. **53**, 1181–1194 (2020). https://doi.org/10.1107/S1600576720009140
12. Smith, M.C., Smith, A.C., Ohms, C., Wimpory, R.C.: The NeT Task Group 4 residual stress measurement and analysis round robin on a three-pass slot-welded plate specimen. Int. J. Press. Vessel. Piping **164**, 3–21 (2018). https://doi.org/10.1016/j.ijpvp.2017.09.003
13. Petersen, L., Lima, B., Vinícius Puydinger, M., Santos, M.A., Keiler, A., Ribeiro, A., Cerdeira, A., Pavanello, M.A., Inkson, B.J., Leclere, D., Elfallagh, F., Derby, B.: The effect of focused ion beam machining on residual stress and crack morphologies in alumina. J. Phys. Conf. Ser. **26**, 219 (2006). https://doi.org/10.1088/1742-6596/26/1/052
14. Arrazola, P.J., Kortabarria, A., Madariaga, A., Esnaola, J.A., Fernandez, E., Cappellini, C., Ulutan, D., Özel, T.: On the machining induced residual stresses in IN718 nickel-based alloy: experiments and predictions with finite element simulation. Simul. Model. Pract. Theory **41**, 87–103 (2014). https://doi.org/10.1016/j.simpat.2013.11.009

15. Uzun, F., Korsunsky, A.M.: On the analysis of post weld heat treatment residual stress relaxation in Inconel alloy 740H by combining the principles of artificial intelligence with the eigenstrain theory. Mater. Sci. Eng. A **752**, 180–191 (2019). https://doi.org/10.1016/j.msea.2019.03.009
16. Thamburaj, R., Wallace, W., Goldak, J.A.: Post-weld heat-treatment cracking in superalloys. Int. Met. Rev. **28**, 1–22 (1983). https://doi.org/10.1179/imtr.1983.28.1.1
17. Vijayakumar, P., Raja, S., Rusho, M.A., Balaji, G.L.: Investigations on microstructure, crystallographic texture evolution, residual stress and mechanical properties of additive manufactured nickel-based superalloy for aerospace applications: role of industrial ageing heat treatment. J. Braz. Soc. Mech. Sci. Eng. **46**, 1–18 (2024). https://doi.org/10.1007/s40430-024-04940-9
18. Ming, X., Song, D., Yu, A., Tan, H., Zhang, Q., Zhang, Z., Chen, J., Lin, X.: Effect of heat treatment on microstructure, mechanical and thermal properties of selective laser melted AlSi7Mg alloy. J. Alloys Compd. **945**, 169278 (2023). https://doi.org/10.1016/j.jallcom.2023.169278
19. Pramanik, A., Dixit, A.R., Chattopadhyaya, S., Uddin, M.S., Dong, Y., Basak, A.K., Littlefair, G.: Fatigue life of machined components. Adv. Manuf. **5**, 59–76 (2017). https://doi.org/10.1007/s40436-016-0168-z
20. Bai, Y., Guo, T., Wang, J., Gao, J., Gao, K., Pang, X.: Stress-sensitive fatigue crack initiation mechanisms of coated titanium alloy. Acta Mater. **217**, 117179 (2021). https://doi.org/10.1016/j.actamat.2021.117179
21. Li, Y., Chen, J., Wang, J., Shi, X., Chen, L.: Study on the effect of residual stresses on fatigue crack initiation in rails. Int. J. Fatigue **139**, 105750 (2020). https://doi.org/10.1016/j.ijfatigue.2020.105750
22. Barsoum, Z., Barsoum, I.: Residual stress effects on fatigue life of welded structures using LEFM. Eng. Fail. Anal. **16**, 449–467 (2009). https://doi.org/10.1016/j.engfailanal.2008.06.017
23. Li, H.Y., Sun, H.L., Bowen, P., Knott, J.F.: Effects of compressive residual stress on short fatigue crack growth in a nickel-based superalloy. Int. J. Fatigue **108**, 53–61 (2018). https://doi.org/10.1016/j.ijfatigue.2017.11.010
24. Hensel, J., Nitschke-Pagel, T., Dilger, K.: Effects of residual stresses and compressive mean stresses on the fatigue strength of longitudinal fillet-welded gussets. Weld. World. **60**, 267–281 (2016). https://doi.org/10.1007/s40194-015-0284-6
25. Shiga, C., Murakawa, E., Matsuo, Y., Ohsuga, U., Hiraoka, K., Morikage, Y., Yasuda, K.: Fatigue improvement in high-strength steel welded joints with compressive residual stress. Weld. World. **58**, 55–64 (2014). https://doi.org/10.1007/s40194-013-0093-8
26. Tai, M., Miki, C.: Fatigue strength improvement by hammer peening treatment - verification from plastic deformation, residual stress, and fatigue crack propagation rate. Weld. World. **58**, 307–318 (2014). https://doi.org/10.1007/s40194-014-0115-1
27. Digiacomo, G.: Residual stresses in high-strength steel weldments and their dimensional stability during welding and stress relieving. Mater. Sci. Eng. **4**, 133–145 (1969). https://doi.org/10.1016/0025-5416(69)90053-6
28. Atif Shahzad, M., Safaei, B., Sahmani, S., Basingab, M.S., Hameed, A.Z.: Nonlinear three-dimensional stability characteristics of geometrically imperfect nanoshells under axial compression and surface residual stress. Nanotechnol. Rev. **12**(1), 20220551 (2023)
29. Gao, H., Li, X., Wu, Q., Lin, M., Zhang, Y.: Effects of residual stress and equivalent bending stiffness on the dimensional stability of the thin-walled parts. Int. J. Adv. Manuf. Technol. **119**, 4907–4924 (2022). https://doi.org/10.1007/s00170-021-08252-3
30. Uzun, F., Korsunsky, A.M.: Reconstruction of residual stresses in additively manufactured Inconel 718 bridge structures using contour method. Int. J. Adv. Manuf. Technol. **137**, 4573–4582 (2025). https://doi.org/10.1007/s00170-025-15417-x
31. Zhao, X., Munroe, P., Habibi, D., Xie, Z.: Roles of compressive residual stress in enhancing the corrosion resistance of nano nitride composite coatings on steel. J. Asian Ceram. Soc. **1**, 86–94 (2013). https://doi.org/10.1016/j.jascer.2013.03.002
32. Bai, L., Jiang, K., Gao, L.: The influence and mechanism of residual stress on the corrosion behavior of welded structures. Mater. Res. **21**, e20180166 (2018). https://doi.org/10.1590/1980-5373-MR-2018-01660
33. Wang, G., Zhang, Y., Gao, C., Xu, G., Zhao, M.: Effect of residual stress and microstructure on corrosion resistance of carburised 18CrNiMo7-6 steel. Anti-Corros. Methods Mater. **67**, 357–366 (2020). https://doi.org/10.1108/ACMM-02-2020-2260
34. Takakuwa, O., Soyama, H.: Effect of residual stress on the corrosion behavior of austenitic stainless steel. Adv. Chem. Eng. Sci. **05**, 62–71 (2015). https://doi.org/10.4236/aces.2015.51007
35. Akhtar, W., Lazoglu, I., Liang, S.Y.: Prediction and control of residual stress-based distortions in the machining of aerospace parts: a review. J. Manuf. Process. **76**, 106–122 (2022). https://doi.org/10.1016/j.jmapro.2022.02.005
36. Sim, W.M.: Challenges of residual stress and part distortion in the civil airframe industry. Int. J. Microstruct. Mater. Prop. **5**, 446 (2010). https://doi.org/10.1504/IJMMP.2010.037621
37. Xie, D., Lv, F., Yang, Y., Shen, L., Tian, Z., Shuai, C., Chen, B., Zhao, J.: A Review on Distortion and Residual Stress in Additive Manufacturing. Chin. J. Mech. Eng. Addit. Manuf. Front. **1**, 100039 (2022). https://doi.org/10.1016/j.cjmeam.2022.100039
38. Masoudi, S., Amini, S., Saeidi, E., Eslami-Chalander, H.: Effect of machining-induced residual stress on the distortion of thin-walled parts. Int. J. Adv. Manuf. Technol. **76**, 597–608 (2015). https://doi.org/10.1007/s00170-014-6281-x
39. Banks-Sills, L., Boniface, V., Eliasi, R.: Effect of residual stresses on delamination cracks in fiber reinforced composites. Interface Sci. **11**, 339–348 (2003). https://doi.org/10.1023/A:1025152524541
40. Beuth, J.L., Narayan, S.H.: Residual stress-driven delamination in deposited multi-layers. Int. J. Solids Struct. **33**, 65–78 (1996). https://doi.org/10.1016/0020-7683(95)00021-2
41. P. Preve´y, N. Jayaraman, R. Ravindranath Introduction of Residual Stresses to Enhance Fatigue Performance in the Initial Design. In: Volume 2: Turbo Expo 2004. pp. 231–239. ASMEDC 2004
42. James, M.N.: Residual stress influences on structural reliability. Eng. Fail. Anal. **18**, 1909–1920 (2011). https://doi.org/10.1016/j.engfailanal.2011.06.005

43. Uzun, F., Besnard, C., Vaughan, G., Xu, T., Tan, J.-C., Korsunsky, A.M.: A critical evaluation of diffraction strain tomography and contour method by assessing residual elastic strains and quench-induced cracking in a carbon steel bar. Met. Mater. Int. **32**, 164–178 (2026). https://doi.org/10.1007/s12540-025-01976-x
44. Uzun, F., Slim, M.F., Basoalto, H., Liogas, K., Wang, Z.I., Korsunsky, A.M.: Application of strain tomography and contour method to residual stress analysis in additively manufactured CM247LC superalloy parts. Prog. Addit. Manuf. **10**, 8279–8291 (2025). https://doi.org/10.1007/s40964-025-01116-2
45. Uzun, F., Korsunsky, A.M.: Eigenstrain tomography: full-field residual stress reconstruction via polycrystalline diffraction projections. Acta Mater. **24**, 121872 (2025)
46. Uzun, F., Korsunsky, A.M.: FuzzyContact: a generic contact mechanics formulation via a modified penalty method governed by sigmoidal traction law. Tribol. Int. **215**, 111468 (2026). https://doi.org/10.1016/j.triboint.2025.111468
47. Kesavan Nair, P., Vasudevan, R.: Residual stresses of types II and III and their estimation. Sadhana **20**, 39–52 (1995). https://doi.org/10.1007/BF02747283
48. Nasir, N.S.M., Razab, M.K.A.A., Mamat, S., Ahmad, M.I.: Review on welding residual stress. ARPN J. Eng. Appl. Sci. **11**, 6166–6175 (2016)
49. Everaerts, J., Salvati, E., Uzun, F., Romano Brandt, L., Zhang, H., Korsunsky, A.M.: Separating macro- (Type I) and micro- (Type II+III) residual stresses by ring-core FIB-DIC milling and eigenstrain modelling of a plastically bent titanium alloy bar. Acta Mater. **156**, 43–51 (2018). https://doi.org/10.1016/j.actamat.2018.06.035
50. Schajer, G.S.: Practical Residual Stress Measurement Methods. Wiley, Chichester (2013)
51. Korsunsky, A.M., Withers, P.J.: Plastic bending of a residually stressed beam. Int. J. Solids Struct. **34**, 1985–2002 (1997). https://doi.org/10.1016/S0020-7683(96)00141-2
52. Apuzzo, A., Barretta, R., Canadija, M., Feo, L., Luciano, R., Marotti de Sciarra, F.: A closed-form model for torsion of nanobeams with an enhanced nonlocal formulation. Compos. B Eng. **108**, 315–324 (2017). https://doi.org/10.1016/j.compositesb.2016.09.012
53. Doostfatemeh, A., Hematiyan, M.R., Arghavan, S.: Closed-form approximate formulas for torsional analysis of hollow tubes with straight and circular edges. J. Mech. **25**, 401–409 (2009). https://doi.org/10.1017/S1727719100002884
54. Drebushchak, V.A.: Thermal expansion of solids: review on theories. J. Therm. Anal. Calorim. **142**, 1097–1113 (2020). https://doi.org/10.1007/s10973-020-09370-y
55. Daniel, R., Holec, D., Bartosik, M., Keckes, J., Mitterer, C.: Size effect of thermal expansion and thermal/intrinsic stresses in nanostructured thin films: experiment and model. Acta Mater. **59**, 6631–6645 (2011). https://doi.org/10.1016/j.actamat.2011.07.018
56. Chen, G., Bi, J.: The closed form solutions for axisymmetric modeling of thermal stress due to repetitive pulse laser heating. Appl. Math. Model. **58**, 459–472 (2018). https://doi.org/10.1016/j.apm.2018.02.016
57. Reddy, J.N.N.: An Introduction to the Finite Element Method. McGraw-Hill, New York (2005)
58. Sercombe, J., Masson, R., Helfer, T.: Stress concentration during pellet cladding interaction: comparison of closed-form solutions with 2D (r,θ) finite element simulations. Nucl. Eng. Des. **260**, 175–187 (2013). https://doi.org/10.1016/j.nucengdes.2013.03.019
59. Gray, T.G.F., Tournery, F., Spence, J., Brennan, D.: Closed-form functions for elastic stress concentration factors in notched bars. J. Strain Anal. Eng. Des. **30**, 143–154 (1995). https://doi.org/10.1243/03093247V302143
60. Momcilovic, N., Motok, M., Maneski, T.: Stress concentration on the contour of a plate opening: analytical, numerical and experimental approach. J.Theor. Appl. Mech. **51**, 1003–1012 (2013)
61. Wang, C.M., Reddy, J.N., Lee, K.H.: Shear Deformable Beams and Plates. Elsevier, Oxford (2000)
62. Ramaji, I.J., Memari, A.M.: Interpretation of structural analytical models from the coordination view in building information models. Autom. Constr. **90**, 117–133 (2018). https://doi.org/10.1016/j.autcon.2018.02.025
63. Crisafulli, F.J., Carr, A.J., Park, R.: Analytical modelling of infilled frame structures - a general review. Bull. N. Z. Soc. Earthq. Eng. **33**, 30–47 (2000). https://doi.org/10.5459/bnzsee.33.1.30-47
64. Sahin, M., Karadal, F.M., Yaman, Y., Kircali, O.F., Nalbantoglu, V., Ulker, F.D., Caliskan, T.: Smart structures and their applications on active vibration control: studies in the Department of Aerospace Engineering, METU. J. Electroceram. **20**, 167–174 (2008). https://doi.org/10.1007/s10832-007-9130-6
65. Heidari-Rarani, M., Bashandeh-Khodaei-Naeini, K., Mirkhalaf, S.M.: Micromechanical modeling of the mechanical behavior of unidirectional composites – a comparative study. J. Reinf. Plast. Compos. **37**, 1051–1071 (2018). https://doi.org/10.1177/0731684418779441
66. Shabana, Y.M.: A micromechanical model for composites containing multi-layered interphases. Compos. Struct. **101**, 265–273 (2013). https://doi.org/10.1016/j.compstruct.2013.02.008
67. Andrianov, I.V., Danishevs'kyy, V.V., Kalamkarov, A.L.: Micromechanical analysis of fiber-reinforced composites on account of influence of fiber coatings. Compos. B Eng. **39**, 874–881 (2008). https://doi.org/10.1016/j.compositesb.2007.10.002
68. Uzun, F., Korsunsky, A.M.: Residual stress estimation in structures composed of one-dimensional elements via total potential energy minimization using evolutionary algorithms. J. Manuf. Mater. Process. **9**, 292 (2025). https://doi.org/10.3390/jmmp9090292
69. Vinson, J.R.: The Behavior of Sandwich Structures of Isotropic and Composite Materials. Routledge, New York (2018)
70. Carrera, E.: Theories and finite elements for multilayered plates and shells: a unified compact formulation with numerical assessment and benchmarking. Arch. Comput. Methods Eng. **10**, 215–296 (2003). https://doi.org/10.1007/BF02736224
71. Withers, P.J., Bhadeshia, H.K.D.H.: Residual stress Part 1 - measurement techniques. Mater. Sci. Technol. **17**, 355–365 (2001). https://doi.org/10.1179/026708301101509980
72. Steinzig, M., Takahashi, T.: Residual stress measurement using the hole drilling method and laser speckle interferometry Part IV: measurement accuracy. Exp. Tech. **27**, 59–63 (2003). https://doi.org/10.1111/j.1747-1567.2003.tb00141.x
73. Korsunsky, A.M.: A Teaching Essay on Residual Stresses and Eigenstrains. Butterworth-Heinemann, Oxford, United Kingdom (2017)
74. Mura, T.: Micromechanics of Defects in Solids. Springer, Netherlands, Dordrecht (1987)

75. Uzun, F., Korsunsky, A.M.: Voxel-based full-field eigenstrain reconstruction of residual stresses. Adv. Eng. Mater. (2023). https://doi.org/10.1002/adem.202201502
76. Faghidian, S.A.: A smoothed inverse eigenstrain method for reconstruction of the regularized residual fields. Int. J. Solids Struct. **51**, 4427–4434 (2014). https://doi.org/10.1016/j.ijsolstr.2014.09.012
77. Huang, J., Guo, K., Liu, X., Zhang, Z.: Residual stress prediction across dimensions using improved radial basis function based eigenstrain reconstruction. Mech. Mater. **185**, 104779 (2023). https://doi.org/10.1016/j.mechmat.2023.104779
78. Ribeiro, R.L., Hill, M.R.: A benchmark fracture mechanics solution for a two-dimensional eigenstrain problem considering residual stress, the stress intensity factor, and superposition. Eng. Fract. Mech. **163**, 313–326 (2016). https://doi.org/10.1016/j.engfracmech.2016.06.007
79. Uzun, F., Korsunsky, A.M.: On the identification of eigenstrain sources of welding residual stress in bead-on-plate Inconel 740H specimens. Int. J. Mech. Sci. **145**, 231–245 (2018). https://doi.org/10.1016/j.ijmecsci.2018.07.007
80. Uzun, F.: Insights into chemo-mechanical yielding and eigenstrains in Lithium-ion battery degradation. Batteries **11**, 465 (2025). https://doi.org/10.3390/batteries11120465
81. Uzun, F., Basoalto, H., Liogas, K., Chen, J., Dolbnya, I.P., Ivan, Z., Korsunsky, A.M.: Voxel-based full-field eigenstrain reconstruction of residual stresses in additive manufacturing parts using height digital image correlation. Addit. Manuf. **77**, 103822 (2023). https://doi.org/10.1016/j.addma.2023.103822
82. Uzun, F., Everaerts, J., Brandt, L.R., Kartal, M., Salvati, E., Korsunsky, A.M.: The inclusion of short-transverse displacements in the eigenstrain reconstruction of residual stress and distortion in in740h weldments. J. Manuf. Process. **36**, 601–612 (2018). https://doi.org/10.1016/j.jmapro.2018.10.047
83. Uzun, F., Lee, T.L., Wang, Z.I., Korsunsky, A.M.: Full-field eigenstrain reconstruction for the investigation of residual stresses in finite length weldments. J. Mater. Process. Tech. **325**, 118295 (2024). https://doi.org/10.1016/j.jmatprotec.2024.118295
84. Kartal, M., Turski, M., Johnson, G., Fitzpatrick, M.E., Gungor, S., Withers, P.J., Edwards, L.: Residual stress measurements in single and multi-pass groove weld specimens using neutron diffraction and the contour method. Mater. Sci. Forum **524–525**, 671–676 (2006). https://doi.org/10.4028/www.scientific.net/MSF.524-525.671
85. Uzun, F., Basoalto, H., Liogas, K., Fares Slim, M., Lik Lee, T., Besnard, C., Ivan Wang, Z., Chen, J., Dolbnya, I.P., Korsunsky, A.M.: Tomographic eigenstrain reconstruction for full-field residual stress analysis in large scale additive manufacturing parts. Addit. Manuf. **81**, 104027 (2024). https://doi.org/10.1016/j.addma.2024.104027
86. Song, X., Liu, W.C., Belnoue, J.P., Dong, J., Wu, G.H., Ding, W.J., Kimber, S.A.J., Buslaps, T., Lunt, A.J.G., Korsunsky, A.M.: An eigenstrain-based finite element model and the evolution of shot peening residual stresses during fatigue of GW103 magnesium alloy. Int. J. Fatigue **42**, 284–295 (2012). https://doi.org/10.1016/j.ijfatigue.2012.01.019
87. Jun, T., Korsunsky, A.M.: Evaluation of residual stresses and strains using the eigenstrain reconstruction method. Int. J. Solids Struct. **47**, 1678–1686 (2010). https://doi.org/10.1016/j.ijsolstr.2010.03.002
88. Prager, W., Hodge, P.G.: Theory of Perfectly Plastic Solids. Wiley, New York (1951)
89. Neal, B.G.: The Plastic Methods of Structural Analysis. Chapman & Hall, London (1956)
90. Johnson, W., Mellor, P.B.: Engineering Plasticity. Van Nostrand Reinhold, London (1973)
91. Chakrabarty, J.: Theory of Plasticity. McGraw-Hill, New York (1987)
92. Yu, T.X., Zhang, L.C.: Plastic Bending: Theory and Applications. World Scientific, Singapore (1996)
93. Sidebottom, O.M., Gebhardt, C.F.: Elastic springback in plates and beams formed by bending. Exp. Mech. **19**, 371–377 (1979). https://doi.org/10.1007/BF02324252
94. Wang, J.L., Fu, M.W., Shi, S.Q., Korsunsky, A.M.: Influence of size effect and plastic strain gradient on the springback behaviour of metallic materials in microbending process. Int. J. Mech. Sci. **146–147**, 105–115 (2018). https://doi.org/10.1016/j.ijmecsci.2018.07.027
95. Dang, Q.K., Chang, P.L., Kuo, S.K., Wang, D.A.: Prediction of springback and residual stress of a beam/plate subjected to three-point bending. J. Mech. Mater. Struct. **13**, 421–441 (2018). https://doi.org/10.2140/jomms.2018.13.421
96. Saleh, R., Ali, G., El-Megharbel, A.: Springback of I-Section beam after pure bending with von Mises criteria. World J. Eng. Technol. **06**, 104–118 (2018). https://doi.org/10.4236/wjet.2018.61006
97. Korsunsky, A.M., Regino, G.M., Nowell, D.: Variational eigenstrain analysis of residual stresses in a welded plate. Int. J. Solids Struct. **44**, 4574–4591 (2007). https://doi.org/10.1016/j.ijsolstr.2006.11.037
98. Korsunsky, A.M.: Variational eigenstrain analysis of synchrotron diffraction measurements of residual elastic strain in a bent titanium alloy bar. J. Mech. Mater. Struct. **1**, 259–277 (2006)
99. Beynon, J.H.: Finite-element modelling of thermomechanical processing. Philos. Trans. R. Soc. A Math. Phys. Eng. Sci. **357**, 1573–1587 (1999). https://doi.org/10.1098/rsta.1999.0390
100. Uzun, F., Daisenberger, D., Liogas, K., Wang, Z.I., Chen, J., Besnard, C., Korsunsky, A.M.: Extended caking method for strain analysis of polycrystalline diffraction debye–scherrer rings. Crystals **14**, 716 (2024). https://doi.org/10.3390/cryst14080716
101. Uzun, F., Papadaki, C., Wang, Z., Korsunsky, A.M.: Neutron strain scanning for experimental validation of the artificial intelligence based eigenstrain contour method. Mech. Mater. **143**, 103316 (2020). https://doi.org/10.1016/j.mechmat.2020.103316